OPTICAL CLEANING OF LITHIUM NIOBATE CRYSTALS

Dissertation
zur
Erlangung des Doktorgrades (Dr. rer. nat.)
der
Mathematisch-Naturwissenschaftlichen Fakultät
der
Rheinischen Friedrich-Wilhelms-Universität Bonn

vorgelegt von

Michael Kösters

aus
Neuwied am Rhein

Bonn 2010

Angefertigt mit Genehmigung der Mathematisch-Naturwissenschaftlichen Fakultät der Rheinischen Friedrich-Wilhelms-Universität Bonn

1. Gutachter:	Prof. Dr. Karsten Buse
2. Gutachter:	Prof. Dr. Karl Maier
Tag der Promotion:	29.01.2010
Erscheinungsjahr:	2010

Contents

1 Introduction **1**

2 Fundamentals **3**
2.1 Lithium niobate crystals 3
2.2 Photorefractive effect 4
2.2.1 One-center model 4
2.2.2 Charge driving forces 5
2.2.3 Space charge fields and refractive index changes . . . 7
2.2.4 Two-center model 10
2.3 Optical damage 10

3 Theoretical considerations **15**
3.1 Idea of the optical cleaning 15
3.2 Basics 18
3.3 Numerical simulations 21
3.4 Static cleaning beam 24
3.5 Moving cleaning beam 25
3.6 Asymmetric cleaning beam 32
3.7 Further insights 35

4 Setups for conducting optical cleaning **39**
4.1 Cleaning with coherent light 39
4.2 Cleaning with incoherent light 42

5 Setups for detection of the cleaning performance **45**
5.1 Absorption measurements 45
5.2 Beam distortion measurements 46
5.3 Measurements of light-induced birefringence changes 47

6 Cleaning of iron-doped lithium niobate crystals **51**
6.1 The crystals 51
6.2 Cleaning with a static light pattern 52
6.3 Cleaning with a moving light pattern 56
6.4 Cleaning with incoherent light 59

7 Cleaning of nominally-undoped lithium niobate crystals **63**
7.1 The crystals 63
7.2 Cleaning with a moving light pattern 64
7.3 Cleaning with an asymmetric light pattern 68

8 Discussion **71**
8.1 Comparison: measured and computed concentration profiles in iron-doped crystals 71
8.2 Challenges for optical cleaning of nominally-undoped $LiNbO_3$ crystals 73
8.3 Optical cleaning versus other crystal refinement methods . . 77
8.4 Outlook 78

9 Summary **81**

Bibliography **83**

Chapter 1

Introduction

Optics is the basis of many scientific and technical innovations. Its importance can be inferred, e.g., from the fact that in the last decade several nobel prizes in physics have been awarded to laureates working in the field of optics: Cornell, Ketterle, and Wieman (Bose-Einstein condensation, 2001), Hall and Hänsch (optical frequency comb, 2005), Kao (low-loss optical fibers, 2009), and Boyle and Smith (charge-coupled device, 2009). Almost all of the awarded breakthroughs have been triggered by the invention of the laser in 1960 [1]. Consequently, the transfer of such inventions to the mass market drives the demand for low-cost, mass-producible laser sources. However, even today some parts of the electromagnetic spectrum, especially in the visible region, are difficult and costly to access with laser sources. Nonlinear optics has been established as the solution for completing the missing parts of the spectrum via frequency mixing processes, e.g., second harmonic generation [2]. Realization of such nonlinear-optical processes relies on the availability of high-quality nonlinear-optical crystals.

One of the most important nonlinear-optical materials is lithium niobate [3, 4]. This is due to its unique combination of physical properties: the ease of fabrication, robustness, transparency in the visible-to-infrared spectrum, good electro-optic and nonlinear-optical properties, and the possibility of ferroelectric domain engineering [5–9].

The main obstacle for a widespread use of lithium niobate crystals in nonlinear optics is optical damage, which is the photorefractive effect (PRE) in its unwanted occurrence [10]. The PRE describes the formation of light-induced refractive index changes upon inhomogeneous exposure of the material [11, 12]. It has been exploited extensively in holographic applications, e.g., for optical data storage and diffractive applications such as wavelength division multiplexing [13–16]. However, the same effect

prevents congruently-melting, nominally-undoped $LiNbO_3$ from becoming the number-one-material for nonlinear-optical applications. The fundamental reason for optical damage in these crystals are photoexcitable electrons trapped at transition metals, which are inherent to the production process at concentration levels of parts per million, or at other deep centers, e.g., polarons or bipolarons [17].

Several techniques have been developed to eliminate optical damage in lithium niobate crystals, some of them are briefly introduced in chapter 2.3 [18–34]. Currently, the most successful method is Mg-doping of the crystals above a certain threshold concentration of several mol% [24–29]. However, each method developed so far comes with its own disadvantages. In the case of Mg-doping the crystal production is more costly and domain engineering is complicated. Furthermore, few methods actually tackle the fundamental reason for optical damage, namely the photoexcitable electrons.

In this thesis we present a new method for optical damage suppression. The novel method uses the bulk photovoltaic effect in lithium niobate crystals to remove the photoexcitable electrons from an illuminated region. Simultaneous heating of the crystal ensures charge compensation by mobile ions. In the end, an optically-cleaned region forms, where optical damage is suppressed. The method is somehow similar to high temperature recording of holograms in intentionally-doped crystals [35, 36]. A corresponding technique has already been suggested for purifying waveguide structures in $LiNbO_3$ crystals [37].

A model of the cleaning process is tested experimentally with slightly iron-doped, congruently-melting crystals. Then, the results for nominally-undoped, congruently-melting samples with very low extrinsic impurity concentrations are presented. Finally, a comparison of the new cleaning treatment with existing techniques for optical damage suppression is given.

Chapter 2

Fundamentals

2.1 Lithium niobate crystals

Lithium niobate crystals ($LiNbO_3$) are birefringent as well as piezo-, ferro-, and pyroelectric at room temperature (Curie temperature $T_C = 1165\,^{\circ}C$ [3]). The crystallographic *c*-axis is parallel to the optical axis [3, 4, 38]. These properties are direct consequences of the crystal structure, which belongs to the point group $3m$ [38], i.e. the structure is invariant under rotations of 120° and exhibits a mirror plane containing the rotation axis. The structure is shown in Fig. 2.1.

The nonsymmetric lattice sites of the Nb^{5+} ions and the Li^{+} ions between the oxygen layers lead to breaking of the symmetry along the optical axis, which is accompanied by a strong spontaneous polarization [5]. The direction of this spontaneous polarization can be inverted by applying a strong electric field [9,39]. This effect enables the so-called domain engineering, i.e. the formation of crystal regions with antiparallel orientations of the spontaneous polarization. It is noteworthy that this inversion of the spontaneous polarization causes a change of the sign of any element of a tensor of odd order [40], in particular for the nonlinear-optical tensor *d*.

The $LiNbO_3$ crystals investigated in this thesis are congruently melting crystals, i.e. the crystals and the melt have the same compositions. This implies a non-stoichiometric crystal composition: congruent $LiNbO_3$ crystals exhibit a Li content of 48.4 mol% [41]. Since overall charge neutrality is required, the remaining Li sites are partly (20 %) filled up with Nb^{5+} ions, yielding a high concentration of intrinsic Nb_{Li} antisite defects [41,42]. Thus the crystals have the composition $Li_{0.96}Nb_{1.01}O_3$.

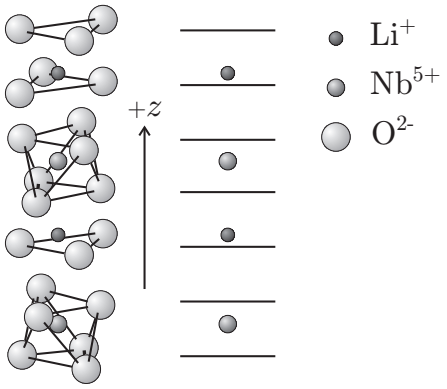

Figure 2.1: Crystal structure of $LiNbO_3$. The orientation of the optical (z-) axis is determined by the displacement of the Li and Nb ions between the oxygen layers.

2.2 Photorefractive effect

In $LiNbO_3$ crystals, local refractive index changes are induced by inhomogeneous illumination. This phenomenon is known as the photorefractive effect: upon illumination, trapped electrons absorb light and are excited from filled charge centers into the conduction band. These electrons are then redistributed and recombine with empty charge centers at a different place. This leads to the build-up of large space charge fields, typically 100 kV/cm, which in turn modulate the refractive index because of the linear electro-optic effect, also called Pockels effect. In this chapter, the principles governing the photorefractive effect are presented based on the one-center charge transport model.

2.2.1 One-center model

Charge transport in $LiNbO_3$ is described using a conventional band scheme with valence band (VB) and conduction band (CB). In fact, $LiNbO_3$ crystals can be considered as excellent insulators because of their band gap of 3.7 eV [43]. Due to this large band gap, the charge transport and the electrical and optical properties of $LiNbO_3$ are greatly determined by charge centers of either intrinsic or extrinsic nature, which are energetically located in the band gap. The intrinsic defects are given by, e.g., Nb_{Li} antisite defects. Extrinsic defects are caused predominantly by transition metal ions (Fe, Cu etc.). They are present in the material either as production impurities in the case of nominally-undoped crystals or as intentional dopants. In both cases, the most prominent species of impurities is iron.

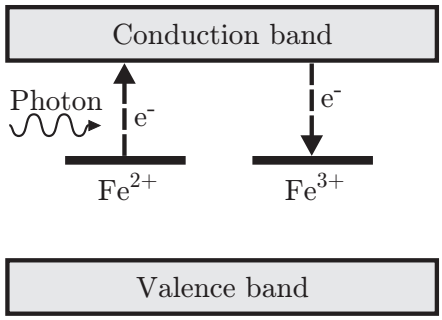

Figure 2.2: Band diagram of the one-center model for $LiNbO_3$ with iron in the valence states Fe^{2+} and Fe^{3+} representing the charge centers. Only excitation of electrons from filled centers (Fe^{2+}) into the conduction band is considered. There, the electrons move before they are trapped by an empty center (Fe^{3+}) located elsewhere.

For intentionally-iron-doped $LiNbO_3$ crystals, the well-known one-center model suits best to describe the charge transport at low light intensities [44]. A sketch is shown in Fig. 2.2. In this one-center model, only one species of deep centers, in our case Fe in the valence states 2+ and 3+ [44, 45], is present and contributes to the charge transport: Fe^{2+} supplies the photoexcitable electrons, Fe^{3+} serves as a trap. Only electronic charge transport via the CB is considered since tunneling between the centers is highly improbable at our doping levels of less than 0.05 mol% [46]. The same is true for hole conduction, which only becomes important for excitation with UV light [47, 48]. Also, at room temperature no thermal excitation of electrons from the iron centers into the CB occurs [35].

Optical excitation from Fe^{2+} into the CB is optimal for photon energies of about 2.5 eV [45]. A typical optical absorption spectrum for iron-doped lithium niobate is shown in Fig. 2.3: a broad absorption band extends from 400 up to 550 nm, which is attributed to the excitation of electrons from Fe^{2+} into the CB. Since the absorption cross section S for this excitation is known to be approximately 5×10^{-18} cm^2 for ordinarily-polarized light at a wavelength of 500 nm [45], it is possible to determine the concentration of Fe^{2+} for a given absorption.

2.2.2 Charge driving forces

Upon excitation into the CB, electrons are subject to several charge driving forces, which are, in general, represented by vectorial current densities. However, in the experiments conducted within this thesis the charge transport and related electric fields are directed predominantly along the

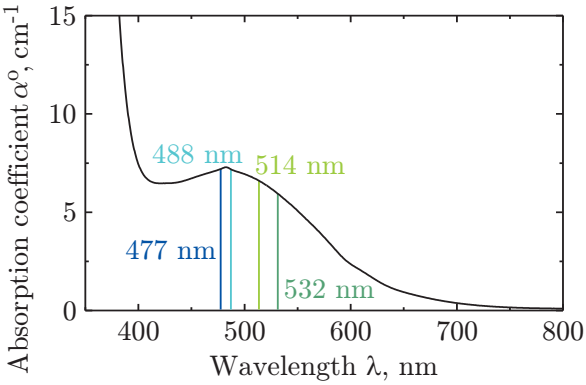

Figure 2.3: Typical absorption spectrum of a $LiNbO_3$ crystal doped with an iron concentration of 2×10^{19} cm^{-3} being in the oxidization state $c_{Fe^{2+}}/c_{Fe^{3+}} \simeq 0.05$: the absorption coefficient for ordinarily-polarized light α^o is shown for different wavelengths λ. The main contribution to the broad absorption band between 400 and 500 nm originates from photoexcitation of electrons from Fe^{2+} centers into the CB.

optical axis of the $LiNbO_3$ crystals, which coincides with the z-axis. We will therefore restrict ourselves to the z-component of the vectorial quantities and use a scalar notation.

For our geometries, the most important charge driving force in $LiNbO_3$ is the bulk photovoltaic effect (PVE) [11,49], which leads to a redistribution of electrons in $LiNbO_3$ upon illumination with a light intensity I. It can be considered as a light-induced drift in the absence of an electric field. The current density, which is attributed to the PVE, is given by:

$$j_{\mathrm{Pv}} = -\beta N_{\mathrm{e}} I \, . \tag{2.1}$$

Here, N_{e} is the concentration of photoexcitable electrons, e.g., $c_{Fe^{2+}}$, and β is the relevant component of the bulk photovoltaic tensor, which is a third-rank tensor with non-zero off-diagonal elements. Conventionally, β is expressed by the photovoltaic shift l_{pv} of an electron per absorbed photon: $\beta = eSl_{\mathrm{pv}}/\hbar\omega$. The shift l_{pv} is typically $0.5 - 1$ Å [11, 49]. For our experiments, the components β_{322} and β_{333} are used.

Drift leads to a charge redistribution according to Ohm's law. Thus, the corresponding drift current density in z-direction is:

$$j_{\mathrm{Drift}} = \sigma E \, . \tag{2.2}$$

Here, σ is the relevant component of the conductivity tensor, which is – due to the trigonal symmetry of $LiNbO_3$ – a diagonal second-rank tensor [50]. The electric field E consists of externally-applied electric fields, space charge fields, and pyroelectric fields [51]. For this thesis, only the space charge field E_{Sc} is of relevance, no external fields are applied.

The conductivity is given by the sum of photo- and dark conductivity: $\sigma = \sigma_{ph} + \sigma_d$ [12]. In the one-center model, the photoconductivity is $\sigma_{ph} = e\mu_e\tau_e S N_e I/\hbar\omega$, where e is the elementary charge, μ_e is the mobility of the electrons and τ_e their lifetime in the CB, S is the photon absorption cross section for photoexcitation from a filled center, e.g., Fe^{2+}, into the CB, and I and ω are the light intensity and frequency, respectively. Generally, the lifetime τ_e depends on N_e. However, this dependence becomes important only when the concentration of empty charge centers is very small. The dark conductivity σ_d has two components: an electronic component, which is due to thermal excitation of electrons, and an ionic component, which is due to thermally-activated, optically-passive ions [52]. As it has been mentioned in the beginning of this section, thermal excitation of electrons can be neglected at room temperature. Because of its low initial value and a thermal activation energy of 1.4 eV it only plays a role for temperatures above 200 °C [35, 53]. Thus, the dark conductivity is dominated by the ionic conductivity [46].

Another charge driving force, which is of minor importance for the overall charge redistribution in our experiments, is diffusion. It can be written as

$$j_{Diff} = k_B T \mu_e \partial_z n_e \,, \tag{2.3}$$

where k_B is Boltzmann's constant, T is the temperature, and n_e is the concentration of electrons in the CB. The latter is given by $n_e \approx S\tau_e I N_e/\hbar\omega$. In general, also μ_e is a second-rank tensorial property [50]. However, as it was the case for the conductivity, only the relevant coefficient for the mobility along the z-axis is needed.

The total current density is given by the sum of bulk photovoltaic, drift, and diffusion current:

$$j_e = j_{Pv} + j_{Drift} + j_{Diff} \,. \tag{2.4}$$

2.2.3 Space charge fields and refractive index changes

Inhomogeneous illumination of a $LiNbO_3$ crystal provides electron redistribution due to the charge driving forces described in the previous sec-

tion. This leads to the build-up of space charge fields E_{Sc}. The process is fully described by a set of three equations: the rate equation for the concentration N_{e}, which describes the excitation of electrons from filled charge centers into the CB and their recombination with empty centers,

$$\frac{dN_{\mathrm{e}}}{dt} = -\frac{SIN_{\mathrm{e}}}{\hbar\omega} + \frac{n_{\mathrm{e}}}{\tau_{\mathrm{e}}} \,, \tag{2.5}$$

the continuity equation,

$$\partial_t N_{\mathrm{e}} = \frac{1}{e}\partial_z j_{\mathrm{e}} \,, \tag{2.6}$$

with j_{e} taken from Eq. (2.4), and the Poisson equation

$$\partial_z E_{\mathrm{Sc}} = -\frac{e}{\varepsilon_z \varepsilon_0}\left(N_{\mathrm{e}} - N_{\mathrm{e}}^0\right) \,. \tag{2.7}$$

In Eq. (2.7), ε_z denotes the corresponding component of the dielectric permittivity tensor, ε_0 is the electric permittivity of the vacuum, and N_{e}^0 refers to the initial concentration of photoexcitable electrons. The concentration n_{e} of electrons in the conduction band is neglected in Eq. (2.7) because it is usually many orders of magnitude smaller than $N_{\mathrm{e}} - N_{\mathrm{e}}^0$.

In the case of a light pattern, whose intensity varies periodically with a grating vector $\vec{K}$ in the z-direction, e.g., an interference pattern of two plane waves, the set of equations can be solved analytically using Fourier analysis [54, 55]. The amplitude of the electric space charge field, i.e. the first order Fourier component, is given by

$$E_{\mathrm{Sc}} = -\frac{E_{\mathrm{Pv}} + iE_{\mathrm{D}}}{1 + E_{\mathrm{D}}/E_{\mathrm{q}} - iE_{\mathrm{Pv}}/E_{\mathrm{q}'}} \,, \tag{2.8}$$

with the bulk photovoltaic field E_{Pv} and the diffusion field E_{D} reading

$$E_{\mathrm{Pv}} = \frac{j_{\mathrm{Pv}}}{\sigma_{\mathrm{ph}}} = \frac{\beta\hbar\omega}{e\mu_{\mathrm{e}}\tau_{\mathrm{e}}S} \qquad \text{and} \qquad E_{\mathrm{D}} = \frac{k_{\mathrm{B}}T}{e}K \,. \tag{2.9}$$

Here, $K = |\vec{K}|$ is the length of the grating vector of the intensity pattern. For a non-periodic intensity pattern, e.g., a single 1-D Gaussian-shaped beam, K is substituted by one over the characteristic length of the light pattern, e.g., the 1/e-radius of the 1-D Gaussian beam. The fields E_{q} and $E_{\mathrm{q}'}$ account for space-charge-limiting effects, when either the filled centers N_{e} or the empty centers $N_{\mathrm{e}}^{\Sigma} - N_{\mathrm{e}}$, where N_{e}^{Σ} is the total concentration of charge centers, e.g., c_{Fe}, are depleted:

$$E_{\mathrm{q}} = \frac{e}{\varepsilon_z\varepsilon_0 K}\left(\frac{1}{N_{\mathrm{e}}} + \frac{1}{N_{\mathrm{e}}^{\Sigma} - N_{\mathrm{e}}}\right)^{-1} \qquad \text{and} \qquad E_{\mathrm{q}'} = \frac{e}{\varepsilon_z\varepsilon_0 K}N_{\mathrm{e}} \,. \tag{2.10}$$

Thus, E_q and $E_{q'}$ represent upper limits for E_{Sc}, which are determined by the amount of available charges N_e and by the effective charge density $\left[1/N_e + 1/(N_e^{\Sigma} - N_e)\right]^{-1}$.

For characteristic lengths of the light pattern > 1 µm and doped crystals with medium oxidization states, the diffusion field and space charge limiting effects can be neglected, so that the steady-state value of the space charge field is equal to the bulk photovoltaic field. This photovoltaic field can reach very high values of up to $10^4 - 10^5$ V/cm, which is due to two reasons: the large photovoltaic coefficients ($\beta_{322,333} \approx (6-7) \times 10^{-27}$ Acm^3/W [38]) and an anomalously low mobility-lifetime product $\mu_e \tau_e$, typically on the order of $10^{-13} - 10^{-12}$ cm^2/V for iron-doped $LiNbO_3$ with $N_e \approx 10^{17} - 10^{19}$ cm^{-3} [11].

However, for very low doping concentrations, such as production impurities on the order of ppm, space charge limitation can come into play and diminish the steady-state value for the space charge field drastically; the final value is then given by the field $E_{q'}$. The same is true for extreme oxidization states as they are realized using the optical cleaning, which will be presented in the following chapters.

The build-up of the space charge field for illumination with a 1-D light pattern is described by an exponential function [54, 55]:

$$E_{Sc}(t) = E_{Pv}\left[1 - \exp(-t/t_d)\right] \ . \tag{2.11}$$

Diffusion as well as space charge limitation are neglected. In this case the steady-state value of the space charge field E_{Sc} is given by the photovoltaic field E_{Pv}. The dielectric relaxation time t_d of the build-up is related to the photoconductivity σ_{ph} by $t_d = \varepsilon_z \varepsilon_0 / \sigma_{ph}$.

For 2-D light intensity patterns, e.g., a 2-D Gaussian beam, the steady-state value of the space charge field remains almost the same, whereas the build-up changes considerably and becomes strongly non-exponential [56].

Due to the linear electro-optic effect [11, 57], the so-called Pockels effect, the build-up of space charge fields E_{Sc} is accompanied by changes of the dielectric permittivity tensor, which is a second-rank tensor [50]. For isotropic probing of these changes, i.e. equally polarized incoming and outgoing probe light, the changes of the dielectric permittivity tensor are nothing else but changes of the ordinary/extraordinary index of refraction $\Delta n_{o,e}$. They can be quantified for a given space charge field E_{Sc} and light

polarization according to:

$$\Delta n_{\mathrm{o,e}} \approx -\frac{1}{2} n_{\mathrm{o,e}}^3 r_{113,333} E_{\mathrm{Sc}} \,, \tag{2.12}$$

where $n_{\mathrm{o,e}}$ is the relevant refractive index, and $r_{113,333}$ is the coefficient of the third-rank electro-optic tensor. It is worth mentioning that the biggest electro-optic coefficient of $LiNbO_3$ is $r_{333} = 32$ pm/V; it is larger by approximately a factor three compared to $r_{113} = r_{223} = 10$ pm/V [58].

Quantitatively, refractive index changes can reach values of more than 10^{-3} due to the very high electric fields mentioned above.

2.2.4 Two-center model

For light intensities higher than 100 W/cm^2, the one-center model is not sufficient to describe the charge transport processes. Therefore, a two-center model has been developed [12, 59]: it assumes the presence of a second, shallow charge center, which is thermally depopulated at room temperature. In $LiNbO_3$, this shallow center is attributed to Nb_{Li} antisite defects with a niobium atom sitting on a lithium site [17, 41, 59]. These defects result from the non-stoichiometry of the crystals (see Section 2.1).

At high light intensities, excitation from deep centers leads to such a large population of electrons in the conduction band that the recombination of electrons with the shallow centers exceeds their thermal depopulation. Since the maximum absorption cross section for optical excitation of electrons from the shallow center is located at a wavelength of 800 nm [17], absorption from these shallows centers is smaller for illumination at a wavelength suitable for the deep center. The electrons trapped in the shallow centers are temporarily lost for the charge transport. Consequently, the photoconductivity does not scale linearly with the light intensity anymore: $\sigma_{\mathrm{ph}} \propto I^x$ with $0 < x < 1$ [12, 59].

There are also indications that optical excitation from the shallow centers is accompanied by a bulk photovoltaic current, presumably with a bulk photovoltaic coefficient, which is larger than the one for the deep center [60–62]. In the end, these changes also affect the steady-state space charge field and, consequently, the refractive index changes [59, 63, 64].

2.3 Optical damage

The undesired appearance of the photorefractive effect and its disadvantageous consequences are called optical damage [10]. This includes macro-

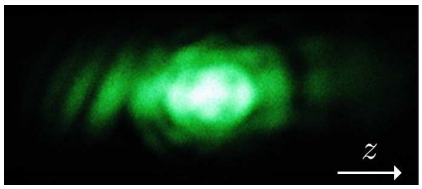

Figure 2.4: A formerly Gaussian-shaped light beam with a light intensity above the critical threshold value for optical damage (total incident power: 2 mW, 1/e-radius: 20 µm, peak intensity: 300 W/cm^2, ordinarily-polarized light) after transmission through a congruent $LiNbO_3$ crystal of thickness $d = 1$ mm: the beam is expanded in an irregular manner, predominantly parallel to the z-axis of the crystal.

scopic beam distortions as well as wavelength-dependent phase shifts, which are both consequences of the light-induced refractive index changes caused by the photorefractive effect.

An example for optical damage is shown in Fig. 2.4: a formerly Gaussian-shaped light beam is expanded in an irregular manner after propagating through a $LiNbO_3$ crystal, predominantly parallel to the z-axis of the crystal, but to some extend also along the y-axis.

There are two main contributions to this distortion [65]: the first one is the formation of a macroscopic lens on the order of the beam size due to the photorefractive effect. The second contribution, which is mostly responsible for the irregular distortion of the beam, arises from holographic scattering: light is scattered from surface or bulk crystal defects and interferes with the main beam leading to refractive index patterns via the photorefractive effect. Diffraction at these patterns may cause an energy transfer from the main beam into the scattered beam parts. This further increases the refractive index changes, scattering is enhanced and so on [66]. Since the electro-optic coefficients are larger for gratings oriented parallel to the z-axis, the beam distortion is stronger in this direction.

In addition, also light absorption can contribute to optical damage [65]: it increases the lensing effect via the thermo-optic effect, which describes changes of the refractive index upon heating of the crystal. The absorption can result from the excitation of electrons from deep centers into the conduction band (blue and green light) or from the excitation of electrons from Nb_{Li} antisite defects (near IR light). The latter absorption mechanism only plays a role for high light intensities in the visible spectrum, when the shallow charge centers are filled. This phenomenon is known as green-light-induced infrared absorption (GLIIRA) [67].

A peculiarity of optical damage is that it appears only if the light inten-

sity exceeds a threshold value. The exact reason for this threshold behavior is not yet clear. There are indications that the second, shallow center is involved and leads to increased refractive index changes [30, 59, 68, 69]. However, the fundamental reason for optical damage should still be photoexcitable electrons, trapped at deep centers.

Methods for optical damage suppression

In the past, several attempts based on improved production techniques have been made in order to get rid of the deep centers, and therewith of the photoexcitable electrons [18]. However, even today it is not possible to reduce the concentration of the most harmful extrinsic defect, namely iron, to less than 1 ppm $\approx 10^{16}$ cm^{-3}. As we will learn in the next chapters, this concentration is still far too high to eliminate optical damage. Therefore, other techniques have been developed to avoid optical damage. A useful overview is found in Ref. 70. Here, some of the most common techniques are described briefly.

We start with a very intuitive technique: instead of growing non-stoichiometric, congruently-melting $LiNbO_3$ crystals, which exhibit a very high concentration of shallow charge centers in the form of intrinsic defects ($\approx 10^{20}$ cm^{-3}), it appears logical to produce crystals, which are very close to stoichiometry and lack such defects. Growth of perfectly stoichiometric crystals has not been achieved so far, but a suppression of optical damage has already been observed for crystals close to stoichiometry, i.e. with a lithium content exceeding 49.9 mol%. These crystals have been realized via two ways: either by special growing techniques or by refining congruent starting material with the help of a vapor-transport-equilibration [19–23].

The most successful state-of-the-art technique for optical damage suppression is doping of congruently-melting $LiNbO_3$ crystals with Mg above a threshold concentration of 5.5 mol% [24, 25]. The Mg atoms replace the Nb_{Li} antisite defects and occupy Li vacancies. Thereby, the concentration of Nb_{Li} defects is strongly reduced. The photoconductivity and also the dark conductivity are enhanced [25, 71, 72]. In the absence of space charge limitation and neglecting diffusion, i.e. when the steady-state space charge field is given by $E_{Sc} = j_{Pv}/(\sigma_{ph} + \sigma_d)$, this treatment decreases the achievable refractive index changes. Similar results have been obtained for other dopants like zinc, indium, scandium, hafnium, and zirconium, each requiring different doping levels in the mol%-range. The impact of the doping can even be enhanced if it is applied to crystals with a com-

position close to stoichiometry. In this case also lower doping levels are sufficient [26–29].

A third method for optical damage suppression is operation of the nonlinear-optical crystals at elevated temperatures of $150 - 200\,^{\circ}\mathrm{C}$ [30,31]. As we will see in the following chapter, both contributions to the conductivity, σ_{ph} and, in particular, σ_{d} are thermally activated. Thus the overall conductivity at the elevated temperatures is strongly increased, again leading to a decrease of E_{Sc}.

Last but not least, the thermo-electric oxidization should be mentioned, which has been developed by *Falk et al.*. It directly attacks the fundamental reason for optical damage: the photoexcitable electrons [32–34]. With the help of a treatment combining an external electric field and high temperatures of $\approx 700\,^{\circ}\mathrm{C}$, these electrons are thermally excited into the CB and then pulled out of the crystal at the positive electrode due to the field induced drift. In order to ensure charge neutrality of the crystal, ionic compensation charges leave the crystal at the opposite electrode [73].

Chapter 3

Theoretical considerations

3.1 Idea of the optical cleaning

In this chapter, a new method for the suppression of optical damage in $LiNbO_3$ – the optical cleaning – is introduced. It is based on drastically reducing the amount of photoexcitable electrons, which are the origin of optical damage. As soon as this reduction is accomplished, the maximum value for the light-induced electric field should be strongly decreased by space charge limitation. Thus, the corresponding refractive index changes should remain on a level small enough to avoid optical damage, i.e. on the order of 10^{-5} or below. Given that the maximum space charge field in this situation is determined by $E_{q'} = ewN_e/\varepsilon_z\varepsilon_0$, we come to a simple estimate for the required reduction of the photoexcitable electrons:

$$wN_e \leq 10^{10}\ \mathrm{cm}^{-2}\ . \tag{3.1}$$

For typical beam radii $w \approx 100$ µm in nonlinear-optical applications, we calculate a concentration $N_e \leq 10^{12}\ \mathrm{cm}^{-3}$. This is a very low value. Even nominally-undoped $LiNbO_3$, which contains remnant impurities only on the ppm level, exhibits concentrations $N_e \approx 10^{15} - 10^{16}\ \mathrm{cm}^{-3}$ (see also Table 7.1). Thus, a reduction of the electron concentration by 3 – 4 orders of magnitude is required to eliminate the part of optical damage, which is due to the photorefractive effect. According to the theoretical considerations, which will be presented in this chapter, this goal can be accomplished by optical cleaning. Additionally, the optical cleaning also fights the thermo-optic contribution to the optical damage: removal of the photoexcitable electrons also lowers the absorption and related heating of the sample upon exposure.

Figure 3.1 shows the basic principle of optical cleaning: the crystal is illuminated with a light pattern $I(z)$ (1). Photoexcitable electrons trapped

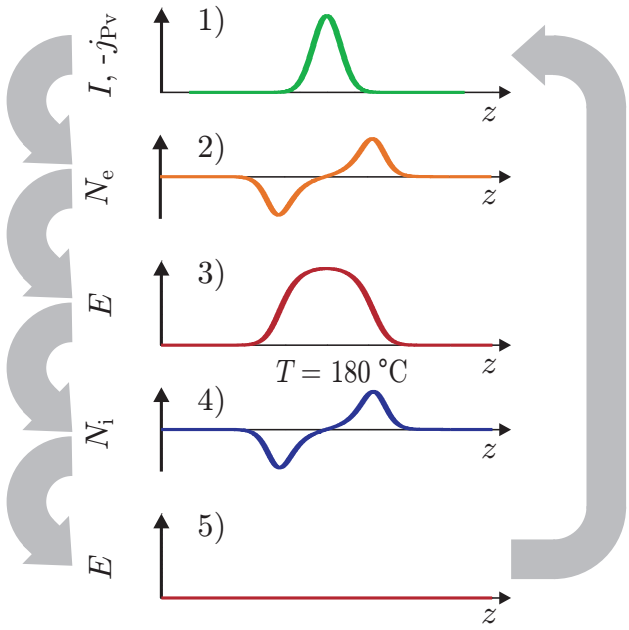

Figure 3.1: Optical cleaning mechanism: upon illumination of a $LiNbO_3$ crystal with an intensity pattern $I(z)$ (1), the bulk photovoltaic current j_{Pv} leads to a redistribution of photoexcitable electrons N_e along the z-axis (2). The accumulating space charge generates an electric field E (3), which stops further redistribution of electrons at room temperature. However, at $180 - 200$ °C optically-passive ions, such as H^+, with a concentration N_i compensate the electronic space charge (4), diminish the blocking electric field E (5) and allow further redistribution of electrons (1). An optically-cleaned region with a very low concentration of photoexcitable electrons is generated.

at defect sites are excited and pushed out of the illuminated region in $+z$-direction (2) due to the bulk photovoltaic effect, which is the dominating charge driving force in this geometry. At room temperature, the redistribution stops quickly because of the build-up of strong space charge fields E (3) and related drift currents, which balance the photovoltaic current. For optical cleaning, however, the crystals are heated to elevated temperatures of $180 - 200$ °C during illumination. At these temperatures, highly-mobile ions like H^+ compensate the electronic charge distribution (4) and inhibit the build-up of strong blocking space charge fields (5). Consequently, further redistribution of electrons caused by the bulk photovoltaic effect is possible (1-2), leading to a cleaned crystal region with a very low concentration of photoexcitable electrons and, thus, with an increased optical damage resistance. Conservation of the cleaned region is achieved

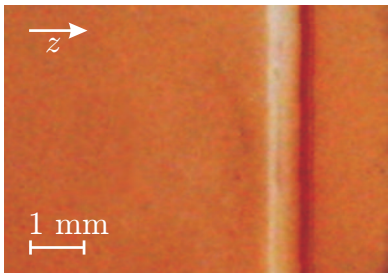

Figure 3.2: Picture of an iron-doped crystal, which has been subjected to a preliminary cleaning experiment with a stripe-like intensity pattern. Whereas the untreated crystal parts show the typical orange color caused by Fe^{2+} ions, the cleaned region is almost transparent, indicating a strongly decreased concentration of photoexcitable electrons trapped at Fe^{2+} ions. In $+z$-direction relative to the cleaned region, the photoexcitable electrons are agglomerated forming more Fe^{2+}. Hence, absorption is stronger there.

either by using only the cleaned region for any follow-up application or by simply cutting off the dirty region, where the photoexcitable electrons are agglomerated.

Figure 3.2 shows a picture of an iron-doped crystal, which was used for preliminary cleaning experiments. The orange color is caused by Fe^{2+} ions (see Section 2.2). At the position of the stripe-like cleaning beam a cleaned region has formed, which is almost transparent: most of the photoexcitable electrons, which were trapped at Fe^{2+} ions, have been removed. Relative to the cleaned region in $+z$-direction, the photoexcitable electrons agglomerate leading to an increased concentration of Fe^{2+}.

An approach similar to the optical cleaning has already been used to increase the optical damage threshold of waveguide structures in $LiNbO_3$ crystals [37]. Furthermore, the method of optical cleaning is strongly linked to high temperature recording of holograms, also known as thermal fixing [35, 36]. However, the purposes and the scalings are entirely different for the optical cleaning: thermal fixing is used to store information in the form of refractive index changes persistently, whereas optical cleaning suppresses the development of such refractive index changes. In order to achieve high storage densities with thermal fixing the refractive index modulations, and thus the generating light intensity patterns vary on the (sub-) micrometer scale. On the contrary, the optical cleaning employs intensity patterns with characteristic widths of $10 - 100$ µm, and the cleaning treatment takes up to several days.

3.2 Basics

Starting from a more detailed look onto the basics of the optical cleaning, we will proceed to more elaborated cleaning scenarios, which provide drastic reduction of the amount of unwanted photoexcitable electrons and thus strong resistance to optical damage.

As it has been explained in the last chapter, photoexcitation and subsequent redistribution of electrons in $LiNbO_3$ can be described using three major charge driving forces: the bulk photovoltaic effect, drift, and diffusion. For the total current density upon illumination of a $LiNbO_3$ crystal with an intensity pattern $I(z,t)$ varying only in z-direction, we get based on Eqs. (2.1)-(2.4):

$$j_\mathrm{e} = -\beta N_\mathrm{e} I + e\mu_\mathrm{e}\left(n_\mathrm{e}E + \frac{k_\mathrm{B}T}{e}\partial_z n_\mathrm{e}\right) . \tag{3.2}$$

Due to the chosen geometry, charge transport predominantly occurs along the z-axis of the crystal, i.e. $j_\mathrm{e} = j_\mathrm{e}(z,t)$, $n_\mathrm{e} = n_\mathrm{e}(z,t)$, and $E = E(z,t)$. Furthermore, the diffusion contribution to j_e is negligible compared to the other charge driving forces unless the spatial profile $N_\mathrm{e}(z)$ strongly varies on a sub-micrometer scale. Nevertheless, retaining of the diffusion current density is important to enable numerical calculation of certain cleaning scenarios presented later on.

Since the optical cleaning is executed at elevated temperatures of $180 - 200$ °C, it is necessary to consider the thermal behavior of the relevant electronic properties: the bulk photovoltaic coefficient β grows only very little in the temperature range $25 - 200$ °C [44]. The photoconductivity $\sigma_\mathrm{ph} = e\mu_\mathrm{e}\tau_\mathrm{e}SN_\mathrm{e}I/\hbar\omega$ is thermally activated via the product $\mu_\mathrm{e}\tau_\mathrm{e}$, which follows an Arrhenius law $\mu_\mathrm{e}\tau_\mathrm{e} = (\mu_\mathrm{e}\tau_\mathrm{e})_0 \exp(-e\epsilon_\mathrm{e}/k_\mathrm{B}T)$ with an activation energy ϵ_e of (0.16 ± 0.05) eV [11,74].

The second type of charge carrier, which is necessary for charge compensation – a prerequisite for efficient optical cleaning –, is given in the form of optically-passive ions. In $LiNbO_3$, they are identified with H^+ for temperatures below 200 °C [35,75,76]. Typical concentrations of hydrogen ions are on the order of $10^{18} - 10^{19}$ cm^{-3}. For dehydrogenated crystals, Li^+ ions take over [52]. The ionic current density is given by:

$$j_\mathrm{i} = e\mu_\mathrm{i}\left(N_\mathrm{i}E - \frac{k_\mathrm{B}T}{e}\partial_z N_\mathrm{i}\right) . \tag{3.3}$$

Here, $\sigma_\mathrm{i} = e\mu_\mathrm{i}N_\mathrm{i}$ is the ionic conductivity with μ_i being the ionic mobility and N_i being the ion concentration, respectively. The mobility μ_i is linked

to the diffusion coefficient D_i via the Einstein relation $D_\mathrm{i} = \mu_\mathrm{i} k_\mathrm{B} T/e$. This diffusion coefficient follows an Arrhenius law: $D_\mathrm{i} = D_\mathrm{i}^0 \exp(-e\epsilon_\mathrm{i}/k_\mathrm{B}T)$. Values of the pre-exponential factor D_i^0 are $0.1 - 3$ cm^2/s, the activation energy ϵ_i lies between $1.1 - 1.2$ eV for iron-doped $LiNbO_3$ crystals and between $1.2 - 1.35$ eV for nominally-undoped crystals [52,76,77]. The second contribution to the ionic current density, the ionic diffusion component, can be neglected. It is far less important than the electronic one.

Complete modeling of the optical cleaning requires modifications of Eqs. (2.6) and (2.7) used to describe the photorefractive effect. First, the continuity equation (2.6) for electronic charge transport has to be supplemented by the one for ionic charge transport. Thus we have the two continuity equations,

$$\partial_t N_\mathrm{e} = \frac{1}{e}\partial_z j_\mathrm{e} \quad \text{and} \quad \partial_t N_\mathrm{i} = -\frac{1}{e}\partial_z j_\mathrm{i} \,, \tag{3.4}$$

with the current densities given by Eqs. (3.2) and (3.3). Second, the Poisson equation has to be modified to account for the ionic charges:

$$\partial_z E = \frac{e}{\varepsilon_z \varepsilon_0}\left(N_\mathrm{i} - N_\mathrm{e} - N_\mathrm{i}^0 + N_\mathrm{e}^0\right) \,, \tag{3.5}$$

where $N_\mathrm{e,i}^0$ are the initial concentrations of photoexcitable electrons and compensating ions. It is worth mentioning that the concentrations N_e and N_i are coupled to each other only via the field dependent components of the electronic current density j_e and the ionic current density j_i.

In order to learn about some fundamental aspects of the optical cleaning we will now turn to an exemplary cleaning scenario with a static rectangularly-shaped light pattern, i.e. $I = I_0 = \text{const}$ and $\sigma_\mathrm{ph} = \sigma_\mathrm{ph}^0 = \text{const}$ inside the illuminated region of width z_0 in the z-direction and zero outside of it (see Fig. 3.3). The initial electron and ion concentrations shall be spatially uniform: $N_\mathrm{e,i}(z, t = 0) = N_\mathrm{e,i}^0$. Diffusion of electrons and ions is neglected.

In this scenario, the photovoltaic current $j_\mathrm{Pv} = -\beta N_\mathrm{e}^0 I$ leads to an accumulation of electrons at the $+z$-border of the illuminated region, inducing positive charges at the $-z$-border. The electric field is uniform in the illuminated region. Shortly after switching on the light, the system reaches an electrical equilibrium, where the electronic current $j_\mathrm{e} = j_\mathrm{Pv} + \sigma_\mathrm{ph} E$ and the ionic current $j_\mathrm{i} = \sigma_\mathrm{i} E$ are almost equal, so that the total current $j = j_\mathrm{e} + j_\mathrm{i}$ is practically zero. This happens on a timescale com-

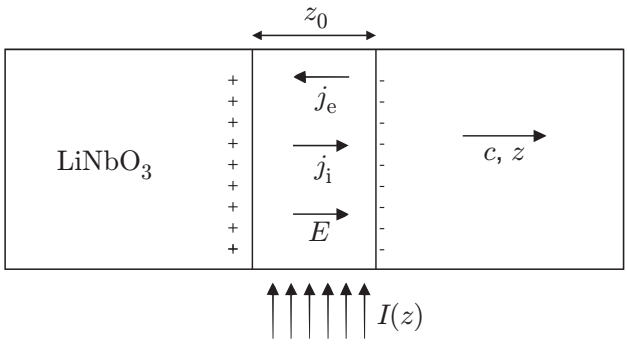

Figure 3.3: Cleaning scenario with a rectangularly shaped light pattern $I(z)$. Even for the quasi-electrical equilibrium, which evolves shortly after switching on the light, the electric field E as well as the current densities j_e and j_i are non-zero.

parable to the dielectric relaxation time $t_d = \varepsilon_z \varepsilon_0 / (\sigma_{ph}^0 + \sigma_i^0)$. The electric field is then given by $E = E_{Pv}/(1 + \sigma_i^0/\sigma_{ph}^0)$, the corresponding currents are $j_{e,i} = \mp j_{Pv}/(1 + \sigma_{ph}^0/\sigma_i^0)$. These currents become maximum for $\sigma_{ph}^0/\sigma_i^0 \ll 1$, when the electric field $E \ll E_{Pv}$ is minimum, i.e. does not block further electron redistribution. For $\sigma_{ph}^0/\sigma_i^0 \geq 1$, which is the case at room temperature, the blocking field $E \simeq E_{Pv}$ becomes very strong and reduces the currents to a minimum. This explains, why the optical cleaning works best at elevated temperatures: whereas the electronic conductivity rises only by a factor 20 from room temperature to $180 - 200\,^\circ$C, the ionic conductivity increases by seven orders of magnitude, providing good charge compensation. Above 200 °C, thermal excitation of electrons sets in, reducing the efficiency of the optical cleaning [35, 53].

Please note, that for $\sigma_{ph}^0/\sigma_i^0 \ll 1$ the electric "equilibrium" is accompanied by large fluxes of electrons and ions. Hence, it is not a true equilibrium, but a quasi-equilibrium. First, electrons from the $-z$-border of the illuminated region are removed and a cleaned region forms. With ongoing cleaning, the concentration at the $-z$-border continuously decreases and the cleaned region grows in $+z$-direction until it reaches the $+z$-border of the illuminated region. In this scenario, the cleaning degree, i.e. the remnant concentration of photoexcitable electrons, is just a question of the applied dosis. Eventually, all photoexcitable electrons can be removed from the illuminated region, given that the total amount of compensating ions is big enough: $N_i^0 \gg N_e^0$.

The characteristic cleaning time t_0 of the cleaning process is given by

$$t_0 = z_0/v_0 \,, \tag{3.6}$$

where z_0 is the width of the illuminated crystal region and v_0 is the photovoltaic drift velocity:

$$v_0 = j_{\mathrm{Pv}}/eN_{\mathrm{e}}^0 = \beta I_0/e = Sl_{\mathrm{pv}}I_0/\hbar\omega \,. \tag{3.7}$$

For $LiNbO_3$, realistic times $t_0 = z_0\hbar\omega/Sl_{\mathrm{pv}}I_0$ are on the order of several hours for a cleaned region of 1 mm width and a medium light intensity of 100 W/cm^2. The characteristic cleaning time t_0 can also be related to the dielectric relaxation time t_{d} via $t_0/t_{\mathrm{d}} \approx E_{\mathrm{q}}/E_{\mathrm{Pv}}(1+\sigma_{\mathrm{ph}}^0/\sigma_{\mathrm{i}}^0)$. This shows that the quasi-equilibrium works very well in the absence of space charge limitation and for an ionic conductivity exceeding the photoconductivity because only then $t_0 \gg t_{\mathrm{d}}$ is valid.

3.3 Numerical simulations

Even though the scenario with a rectangular light pattern presented in the last section was convenient to illustrate some fundamental dependences of the optical cleaning, it cannot be properly realized experimentally. However, realistic scenarios employing an illuminating light beam with, for example, a 1-D Gaussian shape in z-direction complicate an analytical solution of the set of coupled equations (3.4) and (3.5) up to a degree that only numerical solutions remain accessible. This section is dedicated to presenting such a numerical approach. In order to minimize the amount of numerical calculations, the set of equations is first simplified analytically. Therefore, equations (3.4) and (3.5) are reduced to one equation describing the spatio-temporal evolution of the concentration of photoexcitable electrons $N_{\mathrm{e}} = N_{\mathrm{e}}(z,t)$.

With the same justification as it was given for the previous derivations, also the numerical approach is restricted to one dimension, namely the z-direction. Furthermore, we introduce normalized variables:

$$\hat{t} = \frac{t}{t_0} \,, \quad \hat{z} = \frac{z}{z_0} \,, \quad \rho = \frac{N_{\mathrm{e}}}{N_{\mathrm{e}}^0} \,, \quad \hat{E} = \frac{E}{E_{\mathrm{Pv}}} \,, \quad \text{and} \quad \hat{E}_{\mathrm{D}} = \frac{E_{\mathrm{D}}}{E_{\mathrm{Pv}}} \,. \tag{3.8}$$

The light pattern is written in the form $I(\hat{z}) = I_0 f(\hat{z})$. With this notation, f is the normalized driving force of the cleaning, and the continuity equation for the photoexcitable electrons reads:

$$\frac{\partial\rho}{\partial\hat{t}} = \frac{\partial}{\partial\hat{z}}\left(f\rho + \frac{\hat{E}f\rho}{1-c\rho} + \hat{E}_{\mathrm{D}}\frac{\partial}{\partial\hat{z}}\frac{f\rho}{1-c\rho}\right) \,. \tag{3.9}$$

In order to determine the normalized space charge field $\hat{E}$, two assumptions are made: the quasi-electrical equilibrium is active, i.e. $j_e = -j_i$, and $N_e - N_e^0 \simeq N_i - N_i^0$. Then, the electric field $\hat{E}$ arising in the crystal is given by:

$$\hat{E} = \frac{-af\rho + a\hat{E}_D \left(a\frac{\partial \rho}{\partial \hat{z}} - \frac{\partial}{\partial \hat{z}} \frac{f\rho}{1-c\rho} \right)}{1 - b + b\rho + \frac{af\rho}{1-c\rho}} \,. \tag{3.10}$$

Plugging the expression for $\hat{E}$ into Eq. (3.9) we come to one equation describing the change of the concentration of photoexcitable electrons versus time and space:

$$\frac{\partial \rho}{\partial \hat{t}} = \frac{\partial}{\partial \hat{z}} \left[\frac{-f\rho(1-b+b\rho) + \hat{E}_D \frac{\partial}{\partial \hat{z}} \left(\frac{f\rho(1-b+b\rho)}{1-c\rho} \right)}{1 - b + b\rho + \frac{af\rho}{1-c\rho}} \right] \,. \tag{3.11}$$

It includes four dimensionless parameters:

$$a = \frac{\sigma_{ph}^0}{\sigma_i^0}, \quad b = \frac{N_e^0}{N_i^0}, \quad c = \frac{N_e^0}{N_e^\Sigma}, \quad \text{and} \quad \hat{E}_D \,. \tag{3.12}$$

The meaning of these parameters is discussed later on.

For the numerical simulation of the optical cleaning, Eq. (3.11) is discretized in time and space. Since this equation cannot be implemented in an intrinsically stable algorithm, the discretization steps in time and space, $\Delta\hat{t}$ and $\Delta\hat{z}$ have to be chosen carefully to allow stable operation. Typical values for $\Delta\hat{t} \times t_0$ and $\Delta\hat{z}$ are on the order of 1 s and 0.01, respectively.

It is noteworthy that usage of this temporal resolution is only possible due to the formation of the quasi-equilibrium, in which all the involved processes vary with the characteristic cleaning time t_0. Otherwise, the temporal resolution would be related to the dielectric relaxation time t_d, which is about 1000 times smaller for typical experimental cleaning parameters leading to drastically increased computation times.

Now we come back to the relevance of the dimensionless parameters a, b, c, and $\hat{E}_D$: efficient cleaning requires that they are all small compared to one. This case is analogous to that of almost complete ionic compensation ($\sigma_{ph}^0 \ll \sigma_i^0$ and $N_e^0 \ll N_i^0$), a sufficient concentration of empty charge centers ($N_e^0 \ll N_e^\Sigma$), and negligible diffusion.

Whether these conditions are fulfilled in reality depends on the type of crystal and on the experimental conditions. In general, the parameters b, c, and $\hat{E}_D$ fulfill the requirement: the oxidization degree and thus the parameter c can be easily set to $c = N_e^0/N_e^\Sigma < 0.05$, either because this degree

was achieved during crystal growth or because the crystal has been subjected to a conventional oxidization scheme. Typical H^+ concentrations of $10^{18} - 10^{19}$ cm^{-3} also lead to a value $b = N_e^0/N_i^0 < 0.05$ in slightly-doped crystals. For nominally-undoped crystals it is even smaller. The rather large beam radii used for cleaning ensure $\hat{E}_D \ll 1$, typically on the order of 10^{-3}. Experimentally, the most challenging condition is $a = \sigma_{ph}^0/\sigma_i^0 \ll 1$. Since it reflects the ratio of photoconductivity and ionic conductivity, it depends on two experimental parameters: the light intensity I_0 and the temperature T. Decreasing a in the experiment is accomplished most easily by lowering the intensity. — A discussion about the impact of large values for the dimensionless parameters is included in the following sections on optical cleaning with static and moving light patterns, and it is also addressed in the experimental section 6.2 about static cleaning of slightly-doped crystals.

Table 3.1 gives an overview over the standard material parameters for iron-doped $LiNbO_3$ crystals, which, together with the experimental parameters I_0, z_0 and T, are used to determine the dimensionless parameters a, b, c, and $\hat{E}_D$. Where possible, values are also given for nominally-undoped crystals. Unfortunately, such crystals are far less investigated so that these values only serve as guidelines. Unknown values for parameters are filled up with those known from doped crystals or those published in Refs. 68 and 62 (see also Fig. 8.2 in Chapter 8).

Crystal parameter	Iron-doped $LiNbO_3$		Nominally-undoped $LiNbO_3$	
	Value	Refs.	Value	Refs.
β_{322}	6.5×10^{-27} Acm^3/W	[38,78]		
$(\mu_e \tau_e)_0$	1.7×10^{-10} cm^2/V	[11,79]		
ϵ_e	0.16 eV	[11,74]		
S	5×10^{-18} cm^2	[45]		
D_i^0	2.8 cm^2/s	[77]	0.3 cm^2/s	[35,76,77]
ϵ_i	1.17 eV	[77]	1.23 eV	[35,76,77]

Table 3.1: Standard values for the material parameters, which are necessary to determine the dimensionless parameters a, b, c, and $\hat{E}_D$ entering the numerical simulation of the optical cleaning process.

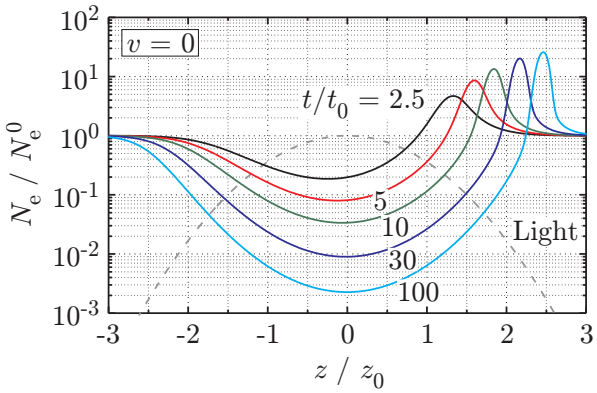

Figure 3.4: Normalized concentration of photoexcitable electrons $\rho = N_e/N_e^0$ versus normalized coordinate $\hat{z} = z/z_0$ for optical cleaning with a static Gaussian-shaped beam ($v = 0$). The profiles are given for different cleaning times $\hat{t} = t/t_0$. The dimensionless parameters are set to $a = c = 0.01$ and $b = \hat{E}_D \ll 1$. The dashed line indicates the position of the cleaning beam.

3.4 Static cleaning beam

The simplest cleaning scenario, which can be realized experimentally, employs a static, Gaussian-shaped cleaning beam ($I(\hat{z}) = I_0 \exp(-\hat{z}^2)$). Figure 3.4 shows the resulting concentration profile of photoexcitable electrons $N_e(\hat{z})$ after different cleaning times $\hat{t}$ for favorable values of the dimensionless parameters a, b, c, and $\hat{E}_D$. The profiles are calculated numerically using the discretized version of Eq. (3.11).

Some general features of the concentration profile are observed: with increasing cleaning time $\hat{t}$, the cleaned region, from which the electrons are removed, becomes broader. In contrast, the dirty region, which is located in $+z$-direction relative to the cleaned region and where the redistributed electrons agglomerate, shrinks in width. This process is accompanied by a strong decrease of the concentration N_e in the cleaned region and a strong increase of the concentration in the polluted region. After the initial formation of the concentration profile, the decrease of the minimum concentration N_e^{min}/N_e^0 becomes roughly proportional to the inverse of the cleaning time t/t_0 (see Fig. 3.5). In other words: at this stage, a reduction of the concentration N_e^{min}/N_e^0 by one order of magnitude takes roughly ten-times as long as it was necessary for the previous one.

It is obvious that cleaning down to the desired purification level for an improved optical damage resistance, which would require $N_e/N_e^0 \simeq 10^{-4}$, is too time-consuming even for these optimum values of the dimensionless

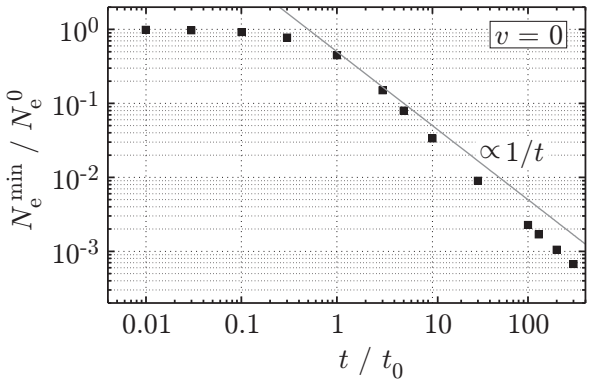

Figure 3.5: Temporal evolution of the minimum concentration of photoexcitable electrons $N_e^{min}(t/t_0)$, normalized to N_e^0, for cleaning with a static Gaussian beam. The values of the dimensionless parameters are $a = c = 0.01$ and $b = \hat{E}_D \ll 1$. The grey line follows a $1/t$ behavior.

parameters: the minimum width to be cleaned in the experiment is $z_0 \simeq 100$ µm. Together with realistic experimental values for the light intensity of $I_0 \simeq 10$ W/cm^2, which are necessary to obtain a small a, this leads to $t_0 \simeq 2500$ s. From Fig. 3.5 we can estimate that $t/t_0 = 10^3 - 10^4$ is necessary to obtain $N_e/N_e^0 \simeq 10^{-4}$, leading to total cleaning times t in the range of $30 - 300$ days.

Experimentally, the simplest way to lower t_0 dramatically is increasing the light intensity I_0. Thus, the question arises whether decreasing $t_0 \propto 1/I_0$ by these means at the expense of an increasing parameter $a \propto I_0$ leads to a drastic reduction of the required cleaning time t without disturbing too much the cleaning process. The answer is given in Fig. 3.6: Mapping N_e^{min}/N_e^0 versus the real cleaning time t we see that the very small characteristic cleaning time t_0 at high light intensities I_0 overcompensates the efficiency losses due to a large a. Hence, for any realization of the optical cleaning with a static cleaning beam optimum values of the dimensionless parameter a should be sacrificed to get small characteristic cleaning times t_0. This favors the usage of rather large cleaning intensities.

3.5 Moving cleaning beam

Now we move on to the next, more sophisticated scenario: optical cleaning with a moving light beam of Gaussian shape. While the maximum

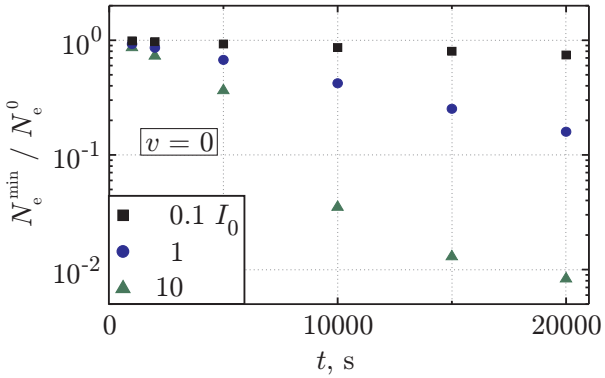

Figure 3.6: Minimum concentration of photoexcitable electrons N_e^{min}, normalized to N_e^0, versus real cleaning time t for cleaning with a static Gaussian beam ($v = 0$). The light intensity is used to increase the parameter $a \propto I_0$ from 0.1 to 10 and, at the same time, to decrease $t_0 \propto 1/I_0$ from 70000 sec to 700 sec. The values of the other dimensionless parameters are $c = 0.01$ and $b = \hat{E}_D \ll 1$.

light intensity I_0 is unaffected by this modification, the function f, which describes the shape of the light beam, now becomes time-dependent:

$$f(\hat{z}, \hat{t}) = \exp\left[-\left(\hat{z} - \frac{v}{v_0}\hat{t}\right)^2\right] . \tag{3.13}$$

Here, v is the moving velocity of the light beam and v_0 is the photovoltaic drift velocity. Including this modification in the discretized version of Eq. (3.11), we can also simulate this cleaning scenario. It is shown in Fig. 3.7 for a moving velocity of $v = 0.6\,v_0 = 6.4$ nm/s. The values of the dimensionless parameters are $a = c = 0.01$, $b = \hat{E}_D \ll 1$. For comparison, the cleaning result for a static cleaning beam is also given.

Two main advantages of using a moving beam become obvious: first, cleaning of larger crystal volumes is possible with this scheme. Second, and rather surprising, the cleaning is strongly enhanced for the moving beam. Already after $t = 10\,t_0$, the minimum concentration N_e^{min}/N_e^0 is decreased by two orders of magnitude more than in the case of a static cleaning beam. Thus, purification levels of $N_e/N_e^0 \simeq 10^{-4}$, which are necessary for an improved optical damage resistance, should be accessible with this scheme.

Is there a way to understand this dramatic cleaning enhancement for the moving cleaning beam? For this purpose, we return to the simple situation with an excessive ionic conductivity $\sigma_i \gg \sigma_e$ and a concentration of ions $N_i \gg N_e$. This is equal to $a = b \simeq 0$. Electronic and ionic diffusion

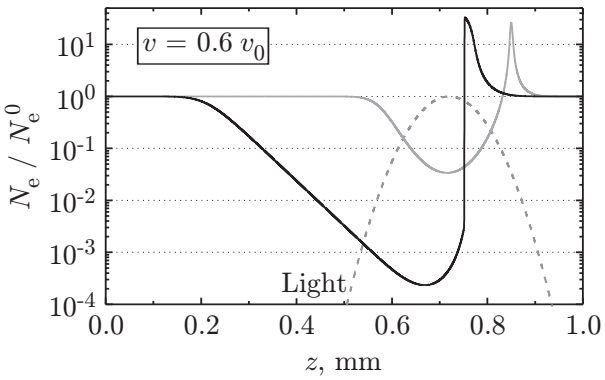

Figure 3.7: Concentration profile $N_e(z)/N_e^0$ after $t = 10\,t_0$ for optical cleaning with a Gaussian-shaped beam moving at a velocity of $v = 0.6\,v_0$ (black line). The dimensionless parameters are set to $a = c = 0.01$, $b = \hat{E}_D \ll 1$. The dashed line indicates the position of the cleaning beam at the end of the cleaning. For comparison, the corresponding profile after $t = 10\,t_0$ for cleaning with a static light beam is also given (grey line).

are neglected, i.e. $\hat{E}_D = 0$. In addition, we transfer to a coordinate frame moving with velocity v. The new spatio-temporal variables now read:

$$\hat{t}' = \hat{t} \qquad \text{and} \qquad \hat{z}' = \hat{z} - \frac{v}{v_0}\hat{t}\,, \tag{3.14}$$

and the driving force f becomes time-independent again. In this situation, Eq. (3.11) can be simplified to

$$\frac{\partial \rho}{\partial \hat{t}'} = \frac{\partial u\rho}{\partial \hat{z}'}\,, \tag{3.15}$$

where $u(\hat{z}') = f(\hat{z}') - v/v_0$ is an effective velocity profile (see Fig. 3.8). It exhibits two zero points $\hat{z}'_{1,2} = \mp\sqrt{\ln(v_0/v)}$ for $0 < v/v_0 < 1$, which are of special importance: electrons with positions $\hat{z}'$ between $\hat{z}'_1$ and $\hat{z}'_2$ exhibit a relative velocity $u > 0$, i.e. they move away from $\hat{z}'_1$ in $+z$-direction towards $\hat{z}'_2$. Those electrons with $\hat{z}' < \hat{z}'_1$ show a negative effective velocity u, they are too slow and move away from $\hat{z}'_1$ in $-z$-direction. In total, all electrons in the vicinity of $\hat{z}'_1$ diverge from it. Similarly, all the electrons in the vicinity of $\hat{z}'_2$ converge on it. Hence, the concentration $\rho = N_e(\hat{z}')/N_e^0$ is minimum and maximum at $\hat{z}'_1$ and $\hat{z}'_2$.

Moreover, Eq. (3.15) can be transformed into a simple differential equation at the zero points $\hat{z}'_{1,2}$:

$$\frac{\partial \rho}{\partial \hat{t}'} - 2\left(\mp\frac{v}{v_0}\sqrt{\ln(v_0/v)}\right)\rho = 0\,. \tag{3.16}$$

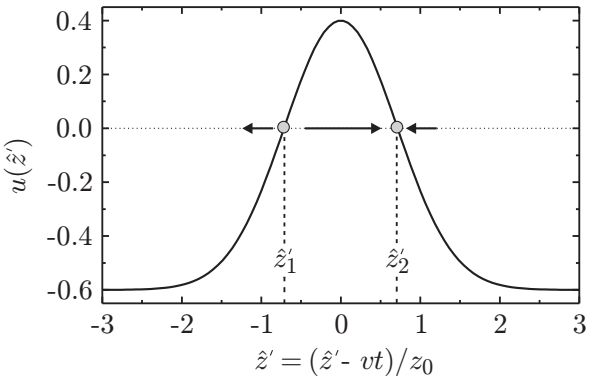

Figure 3.8: Dependence $u(\hat{z}')$ for $v/v_0 \simeq 0.6$. The dots mark the zero points of u, namely $\hat{z}'_{1,2}$. The arrows indicate the directions of motion for the electrons in a coordinate frame moving with velocity v. The dotted line is a guide to the eye for $u = 0$.

Thus, the electron concentration at $\hat{z}'_{1,2}$ decreases/increases exponentially in time. The strength of the exponential decrease/growth is determined by the inverse time constants $\gamma_{1,2} = \mp 2\frac{v}{v_0}\sqrt{\ln(v_0/v)}$, which depend only on the ratio of the velocity v of the cleaning beam and the photovoltaic drift velocity v_0. The absolute values $|\gamma_{1,2}|$ exhibit a maximum $|\gamma_{1,2}|_{\max} \simeq 0.86$ for $v/v_0 \simeq 0.6$ (see Fig. 3.9).

The impact of the velocity ratio v/v_0 on the minimum concentration of electrons $\rho^{\min} = N_e^{\min}/N_e^0$ in the cleaned region is shown in Fig. 3.10. A strong enhancement of the cleaning for optimum values of v/v_0 is obvious already after cleaning times $t = 10\,t_0$. For longer cleaning times, the effect is even more pronounced.

In order to get a better insight on how to tailor the cleaning beam in the experiment, we rewrite the exponent $\gamma_{1,2}\hat{t}'$ in the form

$$\gamma_{1,2}\hat{t}' = (\partial u/\partial \hat{z}')_{1,2}\hat{t}' = -(v_0 t/I_0)(dI/dz)_{1,2}\,. \tag{3.17}$$

This implies that the speed of the exponential cleaning is determined by the slope of the velocity profile u at the zero points. This slope attains its maximum value for $v/v_0 = 0.6$. Clearly, smaller Gaussian widths z_0 lead to a larger exponent. Increasing the intensity does not change the exponent since v_0 is proportional to I_0.

The results of the simple model show very good agreement with those obtained for the numerical simulation with small, but non-zero a, b, c, and $\hat{E}_D$. First, the value for the minimum concentration $N_e^{\min}/N_e^0 = 2.3 \times 10^{-4}$ from Fig. 3.7 agrees very well with the corresponding theoretical value shown in Fig. 3.10. Second, the position of this minimum concentration

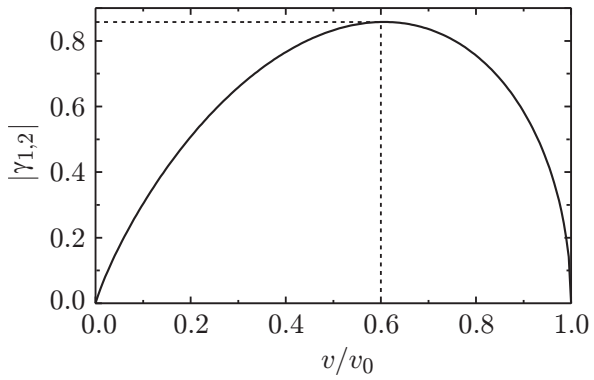

Figure 3.9: Absolute values of the inverse time constants $|\gamma_{1,2}|$ versus the velocity ratio v/v_0 for the moving Gaussian cleaning beam. A maximum value of $|\gamma_{1,2}|_{\max} \simeq 0.86$ is obtained for $v/v_0 \simeq 0.6$.

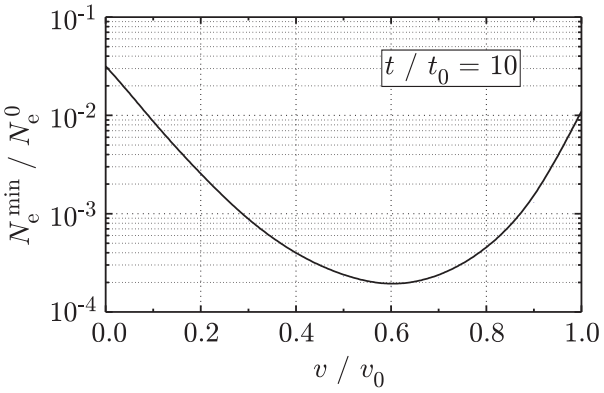

Figure 3.10: Minimum normalized concentration of photoexcitable electrons $\rho^{\min} = N_e^{\min}/N_e^0$ for different ratios v/v_0 within the basic model ($a = b = \hat{E}_D = 0$) after a cleaning time of $t = 10\,t_0$.

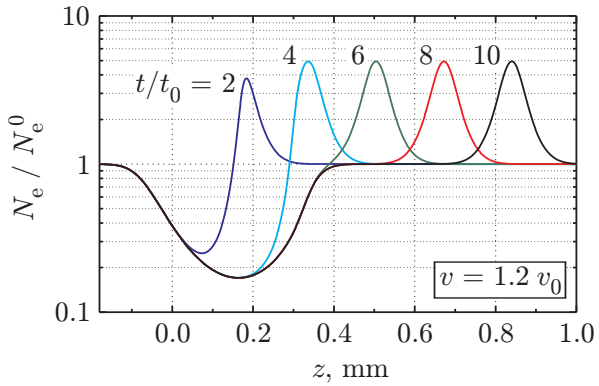

Figure 3.11: Normalized concentration profiles $\rho(z) = N_e(z)/N_e^0$ for cleaning with a moving beam at a supercritical velocity of $v/v_0 = 1.2$ after different cleaning times t/t_0. The profiles are obtained using the simulation based on Eq. (3.11) with the dimensionless parameters set to $a = c = 0.01$, $b = \hat{E}_D \ll 1$. The same parameter values have been used to calculate the profiles in Fig. 3.7.

with respect to the position of the cleaning beam is very close to the expected value of approx. $-0.6\,z_0$. Thus, we can assume that the exponential cleaning occurs for realistic scenarios including imperfect ionic compensation, a limited trap density, and non-zero diffusion.

For $v = 0$ the simple model is not valid anymore, since the increments $\gamma_{1,2}$ become zero. Optical cleaning works in this regime, as it has been shown in the previous section using the numerical simulation, but it does not show the exponential enhancement. The same is true for supercritical velocities $v > v_0$. This scenario can only be simulated numerically. It shows a qualitatively different cleaning behavior: if the velocity is too high, the light beam is spatially separated from the cleaned region and bulldozers only a time-constant amount of electrons in $+z$-direction. In between the cleaned and the polluted region, the concentration of electrons takes on the initial value N_e^0. The cleaning efficiency decreases strongly in the supercritical case. This behavior is illustrated in Fig. 3.11.

What happens if the dimensionless parameters take on large values and, consequently, the perturbations grow? In the interesting region $0 < v < v_0$, noticeable changes of the profile occurring already for small parameter values are a lower peak concentration at $\hat{z}_2'$ and broadening of the polluted region in $+z$-direction, which is predominantly due to the limited trap density N_e^Σ ($\rightarrow c \neq 0$). A second effect is smoothing of the concentration profile in the region around $\hat{z}_2'$. This is caused by the diffusion term in Eq. (3.11) ($\hat{E}_D \neq 0$). If the values increase even more, especially a and

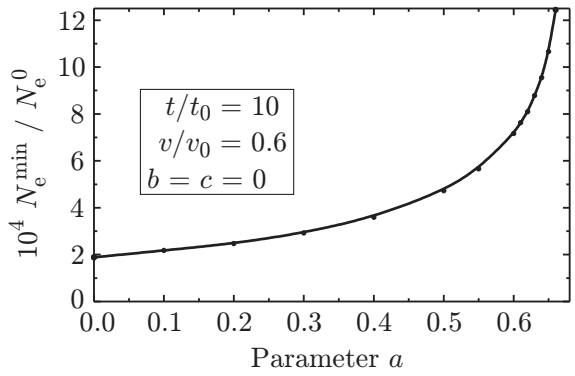

Figure 3.12: Dependence of the minimum concentration N_e^{min}/N_e^0 on the value of the dimensionless parameter a for optical cleaning with a moving beam after a cleaning time $t = 10\,t_0$. The beam velocity is $v = 0.6\,v_0$. The other parameters b, c, and $\hat{E}_D$ are set to zero.

b, also the minimum concentration N_e^{min}/N_e^0 and its position with respect to the light beam are affected. The former is shown in Fig. 3.12 for variation of the parameter a. As long as a stays below $0.3 - 0.4$, the changes of N_e^{min}/N_e^0 are small. However, increasing a further leads to a steep growth of the minimum concentration: the cleaning process is seriously deteriorated. An increase of the parameters b and c has a similar impact.

Please bear in mind though that the results presented in Fig. 3.12 are obtained for solely varying a, while all the other parameters remain constant. Similar to the considerations for cleaning with a static light pattern we can now ask: how does the cleaning process react to an increasing intensity I_0? Since variation of the intensity does not only change the parameter a, but also t_0 and v_0, one has to evaluate the results for absolute times t and velocities v. Due to the increasing photovoltaic drift velocity v_0 for higher light intensities, cleaning of even larger crystal volumes might be possible. A comparison of the minimum concentrations N_e^{min}/N_e^0 versus v and v/v_0 for different cleaning intensities I_0 is given in Fig. 3.13. The cleaning time t used in the simulations is half a day for all the points so that t/t_0 varies from approx. 0.5 to 50 for the different intensities $0.1\,I_0 - 10\,I_0$. The parameter a increases from left to right from 0.065 to 6.5, v_0 lies in the range of approx. $32 - 3200$ µm/day.

The trend is analogous to that shown for the static cleaning: larger intensities give better cleaning for a given time t, even if a takes on large values. Again the effect of cleaning for many characteristic cleaning times t_0 beats cleaning with an optimum value of the parameter a. However, it is evident that for large a the optimum cleaning velocity v is much smaller

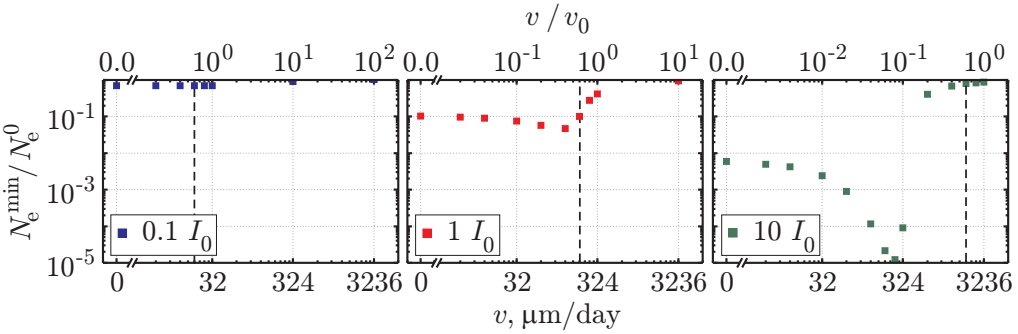

Figure 3.13: Minimum concentration N_e^{min}/N_e^0 after $t = 12$ h versus the real moving velocity v (lower abscissa) and the normalized velocity v/v_0 (upper abscissa) for different cleaning intensities of $0.1\,I_0 - 10\,I_0$. These intensities give from left to right: $t/t_0 \approx 0.5 - 50$, $a \approx 0.065 - 6.5$, and $v_0 \approx 32 - 3200$ µm/day. The other parameters of the cleaning simulation are set to $c = 0.1$, and $b = \hat{E}_D \ll 1$. The dashed black line indicates the position of the optimum cleaning velocity $v = 0.6\,v_0$ as it is expected from the simple model with $a = 0$.

than $0.6\,v_0$. It does not scale linearly with the light intensity I_0 anymore, and breaking of the concentration profile as it is shown in Fig. 3.11 sets in earlier. The decrease of N_e^{min}/N_e^0 still follows the exponential law, but with an inverse time constant γ_1 corresponding to the new optimum velocity. Hence, the decrease is strongly slowed down compared to the situation with $v = 0.6\,v_0$. This is shown more explicitly in Fig. 3.14, where the minimum values N_e^{min}/N_e^0 for the optimum cleaning velocities from Fig. 3.13 are compared with those values obtained from the simple model.

In conclusion, higher intensities are also favorable for the optical cleaning with a moving light beam because a larger crystal volume can be cleaned for a given time and lower minimum concentrations are obtained. However, one has to be careful with the choice of the moving velocity v for $a > 1$ because v_0 does not scale linearly anymore with the intensity and because there is a fine line between optimum and supercritical velocities.

3.6 Asymmetric cleaning beam

Even though optical cleaning with a moving light beam of Gaussian shape has already led to a tremendous enhancement of the cleaning efficiency compared to the scenario with a static light beam, it still suffers from some disadvantageous effects. The most important one is "redirtying" of the cleaned region: it is especially harmful, since the reduction of N_e in the

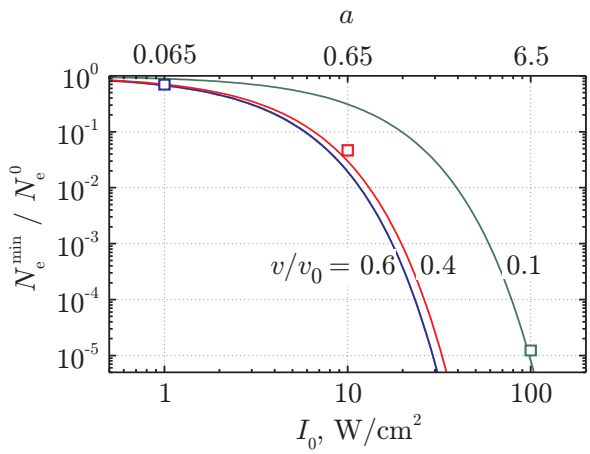

Figure 3.14: Dependence of the concentration N_e^{min}/N_e^0 on the cleaning intensity I_0 for optimum moving velocities v taken from Fig. 3.13 (open symbols). The upper abscissa gives the values of a corresponding to the intensities. For comparison, the solid lines map N_e^{min}/N_e^0 as it is expected from our simple model with $a = 0$.

cleaned region follows an exponential law with $dN_e/dt \propto N_e$ (see Eq. 3.16). Thus, removing the last electrons is very difficult and time-consuming. "Redirtying" is caused by two mechanisms: on the one hand, the trailing edge of the light beam still moves electrons into the already cleaned crystal volume. This effect is suppressed for a very steep trailing edge of the light beam giving a large inverse time constant $|\gamma_1|$. On the other hand, very steep concentration profiles between the two points of minimum and maximum concentration $N_e^{min,max}/N_e^0$, i.e. in between the two zero points $\hat{z}'_{1,2}$, lead to strong diffusion fields, which drag the electrons back into the already cleaned region. This effect is pronounced if the cleaning beam is very narrow so that the points $\hat{z}'_{1,2}$ are close together and the concentration peak at $\hat{z}'_2$ becomes very high. Hence, a large beam diameter can help to solve this problem. For cleaning with a Gaussian-shaped light beam, both detrimental effects have to be balanced by the right choice of the beam diameter.

A possibility for resolving this dilemma is the use of asymmetric light beams with sharp trailing edges, flat tops, and smooth leading edges. In this case Eqs. (3.16) and (3.17) remain valid within the simple model, but with $|\gamma_1| \gg \gamma_2$. The large derivative $dI/d\hat{z}'$ at the trailing edge of the asymmetric beam provides a strong exponential decrease with the rate constant γ_1 for the minimum concentration $N_e^{min}(\hat{z}'_1)$. The flat top widens the cleaned area and ensures a large spatial separation of the points of

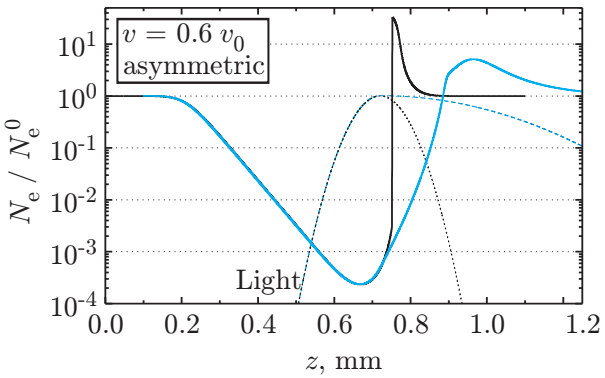

Figure 3.15: Concentration profile $N_e(z)/N_e^0$ (blue line) after $t = 10\,t_0$ for optical cleaning with an asymmetric moving beam, which is composed of two Gaussian edges (blue dashed line). The trailing edge has a 1/e-radius $w_1 = 70$ µm, the leading edge is five-times wider. The parameters for the simulation are set to $a = c = 0.01$, $b = \hat{E}_D \ll 1$, and $v = 0.6\,v_0$. The solid black line describes the corresponding profile after $t = 10\,t_0$ for cleaning with a moving Gaussian-shaped light beam from Fig. 3.7. The Gaussian-shaped beam is also given (black dashed line), its 1/e-radius is equal to that of the trailing edge of the asymmetric beam.

minimum and maximum concentration of the electron profile. Finally, the smooth leading edge broadens the concentration peak in front of the cleaning beam. This broadening is important for cleaning with moving beams: generally, the polluted region around $\hat{z}_2'$ cannot become much larger than the beam radius z_0. Consequently, after moving the beam for $z_0 \times N_e^0/N_e$, the capacity of the polluted region is exhausted and profile breaking sets in. For an asymmetric beam with a smooth leading edge, the capacity is much larger and the beam can be moved for larger distances before profile breaking sets in.

Figure 3.15 shows the concentration profile $N_e(z)/N_e^0$ resulting for a moving asymmetric beam with Gaussian-shaped leading and trailing edges of different widths. The 1/e-radius of the leading edge is five-times bigger than that of the trailing edge. The width of this trailing edge as well as the other parameters of the simulation are the same as for the profiles shown in Fig. 3.7. For $z < 0.7$ mm, the concentration profile overlaps very well with that from Fig. 3.7. The points of minimum and maximum concentration are well-separated now, and the derivative of the concentration profile between these points is drastically decreased. Furthermore, the absolute height of the concentration peak is strongly reduced.

The main advantage of cleaning with an asymmetric light beam is, of course, the possibility to use very sharp trailing edges. Then, the corresponding rate constant $|\gamma_1|$ can be increased even further, leading to a much stronger decrease of the concentration $N_e(z)/N_e^0$ than the one shown in Fig. 3.15. Such sharp trailing edges can be implemented with the help of diffractive elements or by inserting an opaque screen with a sharp edge into a collimated beam. In addition, cleaning with asymmetric light beams is also more robust with respect to large parameters a and c, i.e. to light-induced fields caused by an imperfect ionic compensation and to trap saturation. The former is mainly due to the larger separation of the cleaned and the polluted region, the latter due to the broadening of the concentration peak at the leading edge of the cleaning beam. Breaking of the concentration profile, as it is shown in Fig. 3.11, is also suppressed.

3.7 Further insights

There are other issues related to the optical cleaning process, which are worth mentioning. Some of them are addressed in this section.

Sequential cleaning

The first one is about sequential optical cleaning: multiple cleaning runs performed on the same crystal with a single beam improve the cleaning result if the starting position of the light beam in the second cleaning run is chosen inside the already cleaned region. That way, a disturbing reflow of electrons into the cleaned region by the renewed illumination is inhibited, and even more photoexcitable electrons are removed from the cleaned region.

Cleaning with grating-like intensity patterns

The second issue deals with optical cleaning using a moving, grating-like intensity pattern. There are several arguments in favor of this cleaning scheme, but there are also drawbacks. Positive features are: the grating effectively contains many single beams in a row, which all remove some photoexcitable electrons. In terms of the cleaning efficiency, the situation looks thus similar to the sequential cleaning. In addition, grating structures can be realized with small period lengths on the order of one micrometer resulting in very large gradients dI/dz so that locally very strong cleaning is achieved in short times. However, in order to generate gratings

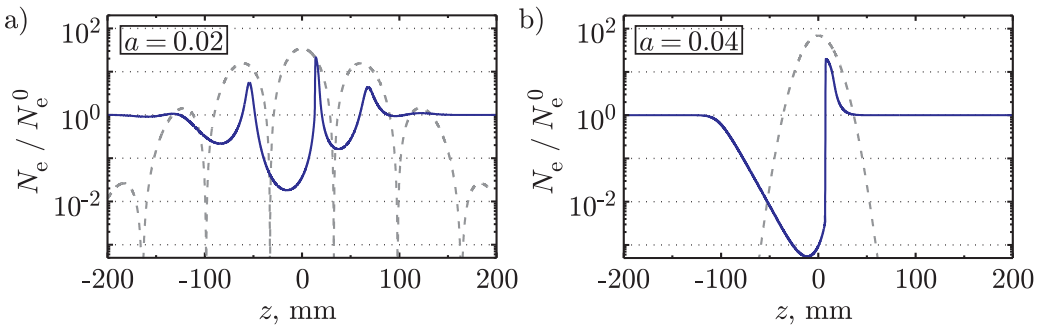

Figure 3.16: Comparison between the concentration profiles $N_e(z)/N_e^0$ (continuous lines) for cleaning with two different intensity patterns (dashed lines) after $t = 4000$ s. The total light power, i.e. the integral over the intensity, is the same. a) A moving, grating-like pattern is used, which is generated by the interference of two plane waves with Gaussian intensity distributions. The grating period is one fourth of the 1/e-radius of the initial beams. b) A single moving Gaussian beam with a diameter similar to the grating period is used. The moving velocities are optimized for both scenarios: for the grating structure it is $v = 0.45\, v_0$, for the Gaussian beam the optimum velocity $v = 0.6\, v_0$ can be used. The parameters b, c, and $\hat{E}_D$ entering the simulation are much smaller than one.

in the experiment, e.g., by interference, focusing of the incident beams is limited. The maximum intensity I_0 is consequently much lower compared to that of a single beam, which is focused to a diameter similar to the grating period. Hence, the cleaning performance of the single beam for a given time t is much better due to a shorter t_0. A comparison of the two cleaning schemes is shown in Fig. 3.16 for a grating structure formed by interference of two plane waves with Gaussian intensity distribution. The grating period is approx. one fourth of the 1/e-radius of the incident beams. The cleaning result for a single Gaussian-shaped beam with a diameter corresponding to the grating period is also given. The initial power, i.e. the integral over the intensity distributions, is the same in both cases.

The better performance of the single beam cleaning is obvious. Even more so, as it gives one continuous cleaned region, whereas the grating structure has to be moved for at least its own extension in z-direction to get a useful cleaned region behind the last intensity peak. The outcome of the comparison might be different, if cleaning with the first intensity peak of the grating structure starts at the $-z$-face of the crystal. Then, each successive intensity peak sees an already lowered concentration of photoexcitable electrons, i.e. the parameter a improves each time. In addition,

"redirtying" of the cleaned region, which is especially harmful if a low concentration N_e/N_e^0 has already been achieved, is kept at a minimum. Nevertheless, such a cleaning scheme involving crystal edges causes a lot of experimental difficulties. Independently of these challenges, the grating structure has to be actively stabilized in the experiment. Altogether, the disadvantages of an inadequate theoretical prediction of the cleaning performance and the experimental challenges for cleaning with grating structures make cleaning with gratings less favorable. Besides, the cleaning results for the simpler scenarios employing moving and/or asymmetric beams are, according to theory, already good enough to suppress the optical damage. Therefore, we will refrain from using grating-like intensity patterns for optical cleaning in this thesis.

Background illumination

A third issue is related to the influence of a constant background illumination during cleaning, which is often unavoidable in the experiment due to scattered light. In the simple model, such a constant offset I_b shifts the effective velocity profile $u(\hat{z}')$ in Fig. 3.8 slightly upwards and pushes the zero points $\hat{z}'_{1,2}$ outwards. Thus, in order to keep the zero points at the previous position, the moving velocity v has to be increased and the optimum moving velocity has to be adapted: $v = (0.6 + I_b/I_0)\, v_0$. The consequences of this velocity shift are considerable: whereas in the simple model without intensity offset, exponential cleaning enhancement with a rate constant $|\gamma_1| > 0$ can be found everywhere in the range $0 < v < v_0$, i.e. over lots of decades in a logarithmic scaling, it is now restricted to $(I_b/I_0)\, v_0 < v < (1 + I_b/I_0)\, v_0$. Depending on the experimental conditions, this can be only one order of magnitude. In the region with $v < (I_b/I_0)\, v_0$, the cleaning scenario is similar to that employing a static cleaning beam. Furthermore, large values for the dimensionless parameters a etc. deteriorate the cleaning earlier and lead to increasing minimum achievable concentrations $N_e^{\min}/N_e^0$.

Chapter 4

Setups for conducting optical cleaning

In this chapter, the setups for optical cleaning are described. The chapter is divided in two sections: the first one is about cleaning with coherent light, i.e. laser light. The second section presents the cleaning setup with high-power LED's as incoherent light sources. The usage of such LED's is possible because optical cleaning does not require coherent light. For an industrial implementation, cleaning with LED's represents a very interesting alternative to cleaning with laser light because both, the initial costs for the light source and the maintenance costs, e.g., due to power consumption, are much lower for LED's.

4.1 Cleaning with coherent light

The important part of the experimental setup for optical cleaning with coherent light is shown in Fig. 4.1. Different lasers can be employed as light sources: an Ar^+ laser with a maximum light power output of 2.8 W at a wavelength of 514 nm, and two Nd:YAG lasers working at a wavelength of 532 nm providing output powers of 80 mW and 5 W, respectively. Using a $\lambda/2$-wave plate and a polarizing beam splitter the intensity of the cleaning light can be adjusted. The ordinarily-polarized light coming out of the beam splitter is used for cleaning.

In order to achieve the large intensity gradients required for efficient optical cleaning, the light beam, whose intensity distribution equals a TEM00 mode, is focused in z-direction using cylindrical lenses of different focal lengths. For the initial 1/e-radius of the laser beam $z_0 \approx 0.7$ mm, the achievable 1/e-focus radii range from 10 – 110 µm. Focusing is done

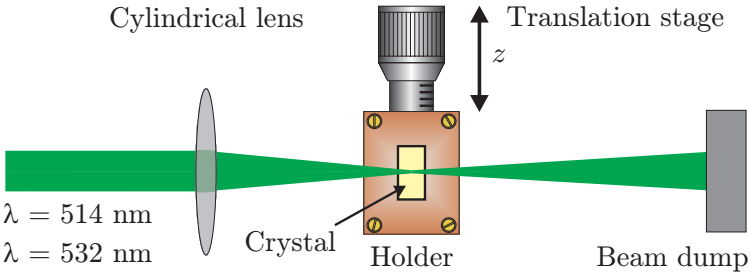

Figure 4.1: Experimental setup for cleaning with coherent light.

taking into account a sufficiently large Rayleigh length with respect to the propagation distance in the crystal. Thus, we can assume an approximately homogeneous intensity over the crystal depth.

The crystal itself is placed in a small furnace, which is mounted on a translation stage. This translation stage allows to move the crystal relative to the light beam with a step width of 0.25 µm.

Two different furnace designs are used: for all experiments with slightly iron-doped $LiNbO_3$ crystals and some with nominally-undoped crystals a simple furnace is used, where the crystal is clamped between two brass plates with heating resistors. The furnace is shown in Fig. 4.2a. The temperature is controlled with a thermocouple in the vicinity of the crystal. In order to increase temperature stability and to reduce thermal losses due to air convection, a special heat-resistive tape is attached around the furnace except for those regions where the light beam enters and exits the holder. Since all the crystals used with this setup have a large x-face of $y \times z = 4 - 5 \times 5 - 6\,\mathrm{mm}^2$ and a small y-face with $x \times z = 1 \times 5 - 6\,\mathrm{mm}^2$, two cleaning geometries are realized, which are sketched in Fig. 4.3: in the first one, the cleaning light impinges on the x-face (Fig. 4.3a). This geometry gives less scattered light off the brass plates and enables the usage of smaller focus radii, but it leads to an inhomogeneous illumination along the y-axis of the crystal. Thus, the cleaning efficiency changes along the y-axis. The second geometry with the cleaning light entering the crystal through the y-face gives a larger propagation length in the crystal (Fig. 4.3b). Thus, more light is used for cleaning, and the intensity along the x-axis shows better homogeneity. In addition, the heated brass plates are closer together, which results in a better temperature control and homogeneity. The accuracy is $\Delta T \leq 1\,^{\circ}\mathrm{C}$. The disadvantage is that there is more scattered light producing unwanted background illumination.

For most of the experiments with nominally-undoped crystals, we used another furnace, which completely surrounds the crystal except for small

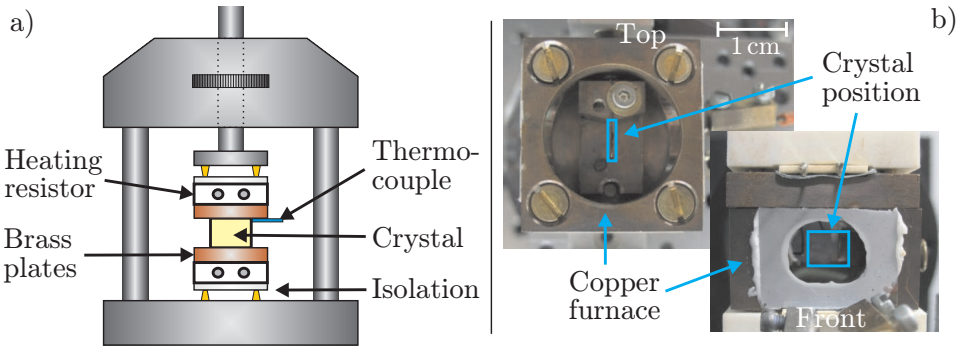

Figure 4.2: a) Holder with a simple crystal furnace: the crystal is clamped between two brass plates, which are heated by resistors. The furnace is thermally isolated from the holder by ceramic isolation. A thermocouple is used to control the temperature. b) Picture of the modified crystal holder, where the brass plates are replaced by a closed furnace with entrance and exit openings for the light. The temperature is again controlled using a thermocouple.

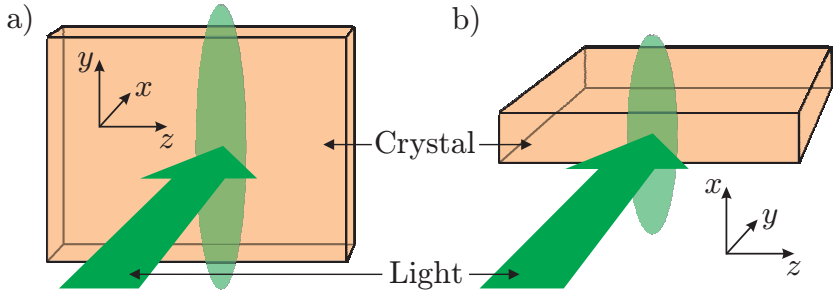

Figure 4.3: Geometries used for optical cleaning: a) the light beam enters the crystal through the x-face, it is polarized along the y-axis of the crystal. b) The light beam enters the crystal through the y-face, it is polarized along the x-axis of the crystal. In both cases, the beam is focused along the z-axis; this is indicated by the elliptical shape of the beam.

entrance and exit holes. The temperature is again controlled by a thermocouple, which can be inserted through a small hole in the side of the furnace. With this design, the temperature homogeneity over the sample and, moreover, the absolute temperature accuracy should be better than with the previous furnace, even when the samples are illuminated standing upright, i.e. through the large x-face. Photographs of this new furnace are shown in Fig. 4.2b. Through a small slit at the side of the furnace, a razor blade can be introduced in the beam path at a distance < 0.5 mm to the crystal surface. This allows to generate asymmetric beam shapes with a Gaussian leading edge and a steep trailing edge with an intensity distribution given by Fresnel diffraction at an opaque half-plane. The razor blade is attached to the optical table. Thus, its position is fixed with respect to the cleaning beam, and the sample can still be moved through the light pattern using the translation stage.

4.2 Cleaning with incoherent light

The proof-of-principle experiments for cleaning with incoherent light are realized using high-power LED's from *Philips*: a Luxeon III Star with an emitting area of 1 mm^2 and a Luxeon V star with an area of 4 mm^2, providing optical output powers of $450 - 600$ mW. The available wavelengths, which allow efficient optical excitation of Fe^{2+}, are 470 and 505 nm. During operation, the LED's are passively cooled.

Although light conversion in these LED's is very efficient compared to a laser, the LED's also exhibit a major disadvantage: they emit extremely divergent light, which is difficult to collimate and, even more so, to focus down to an area smaller than the original emitter area. The opening angle of the light cone is approximately 120 $^\circ$ for the Lambertian emitters used in our experiments. Therefore, two different experimental setups are used with the LED's.

In the first setup, which is sketched in Fig. 4.4a, the light coming from the LED is collimated as good as possible using a combination of a microscope objective and a spherical lens. Then, it is focused onto the crystal using a cylindrical lens in order to obtain a sharp image of the emitter area at the entrance surface of the crystal. The advantage of this setup is that the divergence of the light is reduced. However, almost half of the light is lost to collimation. The second setup does not require any optics. The LED is merely placed as close as possible in front of the crystal, almost touching it. Thus, no losses occur, but the divergence of the light is very strong. The situation is depicted in Fig. 4.4b.

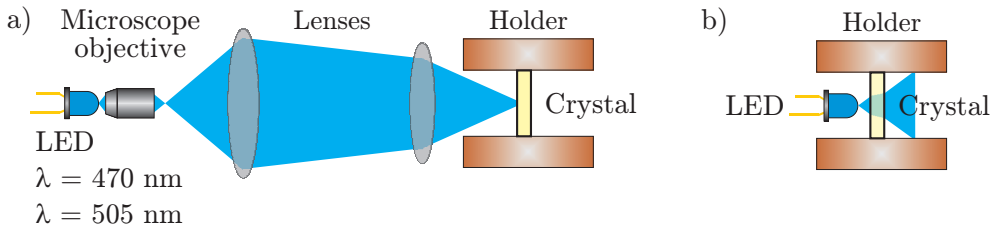

Figure 4.4: Experimental setups for cleaning with incoherent light: a) with collimating and focusing optics; b) the LED is placed directly in front of the crystal, no other optical elements are used.

For both setups, the simple crystal furnace described in the previous section and depicted in Fig. 4.2a is used. The crystals are always illuminated through the x-face (Fig. 4.3a) in order to keep the impact of the large divergence as low as possible.

Chapter 5

Setups for detection of the cleaning performance

In the previous chapter, the setups for conducting optical cleaning have been presented. Now, the setups for detection of the cleaning performance will be introduced. Three different physical mechanisms are used to determine the success of the cleaning: absorption, beam distortion induced by optical damage, and light-induced birefringence changes. The corresponding measurement procedures and experimental setups are described in the following sections.

5.1 Absorption measurements

Measurements of the absorption are the best way for the quantification of the cleaning success since they directly probe the concentration of photoexcitable electrons. For this measurement technique to be applicable, two requirements have to be met: the absorption α has to be directly related to the concentration of photoexcitable electrons, and the absorption cross section or the concentration have to be large enough to give measurable absorption values, i.e. $\alpha d \geq 0.01$ for a given sample thickness d.

As it has been mentioned in Section 2.2, Fe^{2+} exhibits strong absorption in $LiNbO_3$ in the green and blue spectral region. From the absorption $\alpha^{o}_{477\,\mathrm{nm}}$ for ordinarily-polarized light with a wavelength of 477 nm, the Fe^{2+} concentration is determined with good precision using [45]:

$$c_{Fe^{2+}} = (2.2 \pm 0.5) \times 10^{21}\ \alpha^{o}_{477\,\mathrm{nm}}\ . \tag{5.1}$$

Thus, we can estimate the minimum detectable Fe^{2+} concentration to be $c_{Fe^{2+}} \approx 10^{16}\ \mathrm{cm}^{-3}$ for our crystal thicknesses. The corresponding con-

centration in intentionally iron-doped $LiNbO_3$ crystals normally exceeds this minimum value for doping levels of $c_{Fe} \approx 10^{17} - 10^{19}$ cm^{-3}, unless the crystals are prepared in extreme oxidization states. However, for nominally-undoped crystals with impurity concentrations on the order of ppm, i.e. $c_{Fe} \approx 10^{16}$ cm^{-3}, this measurement technique is not applicable.

Thus, the absorption measurements within this thesis are performed only on iron-doped samples. Two different setups are used. For the first one a weak HeNe laser working at a wavelength of 543 nm is coupled into the cleaning setup and focused onto the sample providing a 1/e-radius of 30 µm. Since the sample holder is mounted on a motorized translation stage, it is possible to move the crystal in the z-direction and thus, to obtain a scan of the absorption profile $\alpha(z)$ which has been induced by the optical cleaning. This absorption profile is then calibrated at one point with the absorption at 477 nm to give the spatially-resolved concentration profile $c_{Fe^{2+}}(z) = N_e(z)$.

The second setup measures the absorption in a different way: the sample is inserted into the beam path of a photospectrometer (Cary500 by *Varian*), again mounted on a motorized translation stage. Together with small slit apertures with diameters ranging from 12 to 100 µm, which are placed directly in front of the crystal, this allows to measure the absorption at 477 nm and thus to determine $c_{Fe^{2+}}(z)$. An advantage of the setup with the photospectrometer is that it can be used at the same time to perform spatially-resolved measurements of the H^+ concentration taking advantage of an OH stretching oscillation [77]. From the corresponding absorption $\alpha^o_{2870\ nm}$ at 2870 nm, $c_{H^+}(z) = N_i(z)$ is obtained from:

$$c_{H^+} = (1.7 \pm 0.1) \times 10^{22} \alpha^o_{2870\ nm} \ . \tag{5.2}$$

Evaluation of measurements taken with the two setups described above has to be done carefully: since the width of the light pattern used for the local absorption measurements can be on the order of single features of the investigated absorption profiles, the result of each measurement is a convolution of light pattern and absorption profile. Thus, sharp features of the profile might appear much wider than they actually are, and the relative change of the absorption might be damped.

5.2 Beam distortion measurements

The second technique for determining the success of the optical cleaning is very intuitive with respect to our main goal: the suppression of opti-

cal damage in $LiNbO_3$ crystals. The method makes use of a direct consequence of optical damage, namely the distortion of a regular beam profile for illumination with light above a certain threshold intensity.

The setup is quite simple: a focused beam with a 1/e-radius of 16 μm, coming either from an Ar^+ laser working at $\lambda = 514$ nm or from a Nd:YAG laser working at $\lambda = 532$ nm, is directed onto the sample. The intensity at the crystal is increased stepwise with the help of a $\lambda/2$-wave plate mounted in a motorized rotation stage and a polarizing beam splitter; it can be varied in the range $10^{-3} - 10^4$ W/cm^2. The exposure time for each intensity is $10 - 150$ sec. Only ordinarily-polarized light is used. This reduces the influence of parasitic effects like holographic scattering.

Behind the crystal, the beam is split so that the beam distortion can be measured in two ways: first, a pinhole behind the sample blocks the stray light, which is due to beam distortion, and a photodiode records only the power of the central part of the beam P_{in}. Second, a micro-disc blocks the beam center such that the power of the stray light, P_{out}, is recorded. Both measurement schemes are sketched in Fig. 5.1. The onset of optical damage yields a drastic decrease of P_{in} and a strong increase of P_{out}. The corresponding intensity is taken as the threshold intensity for optical damage. Similar to the setup used for the absorption measurements, the sample is mounted on a motorized translation stage. Therefore, the intensity dependence of the beam distortion can be recorded at different positions along the z-axis of the $LiNbO_3$ crystal. The improvement with respect to optical damage is then given by the ratio χ of the threshold intensity in the cleaned crystal region and the mean threshold intensity of the untreated region. For most of the measurements, only the behavior of P_{out} is analyzed because it is much more sensitive than P_{in}.

5.3 Measurements of light-induced birefringence changes

The third technique used to probe the success of the optical cleaning is based on the generation of light-induced birefringence changes and their detection with a phase compensation method [68, 80].

The idea behind this technique is the following: as we have seen in Chapter 2, inhomogeneous illumination of a $LiNbO_3$ crystal generates large local space charge fields. Such an electric field, oriented along the z-axis of a $LiNbO_3$ crystal, leads to different electro-optic refractive index changes $\Delta n_{\text{o,e}}$ for ordinarily and extraordinarily polarized light. The re-

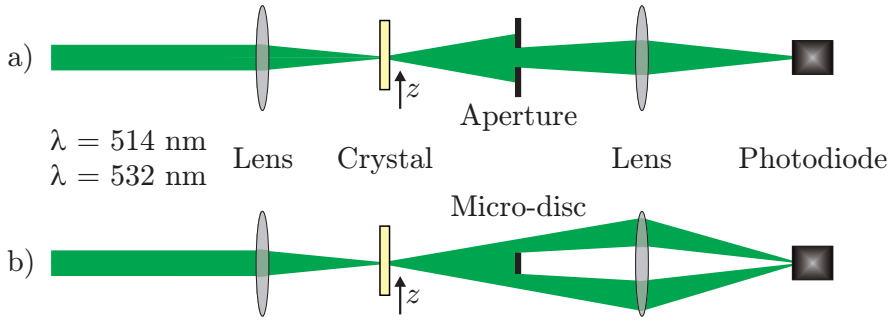

Figure 5.1: Beam distortion measurement: upon the onset of optical damage, the beam transmitted through the $LiNbO_3$ crystal is distorted. This distortion is measured in two ways: a) an aperture blocks the stray light due to the distortion and records only the power of the central part of the beam P_{in}. b) The beam center is blocked and only the stray light P_{out} is recorded.

sulting change of the birefringence is given by

$$\delta n = \Delta n_{\text{e}} - \Delta n_{\text{o}} \, . \tag{5.3}$$

If we were able to reduce the amount of photoexcitable electrons drastically in the optically cleaned region, the birefringence changes would be much smaller in the cleaned region – due to space charge limitation.

Generation and detection of the birefringence changes are realized experimentally with the setup shown in Fig. 5.2: build-up of the electric space charge field and thus of the birefringence changes is accomplished by illumination of the samples with a focused Gaussian beam at the wavelength 532 nm impinging onto the x-face of the crystal. The 1/e-radius at the beam waist is $w_{532} = 21$ µm. The peak intensity can be varied in the range $30 - 30000$ W/cm^2.

A weak Gaussian laser beam at 633 nm with a 1/e-radius at the beam waist of $w_{633} = 15\,\mu$m and a peak intensity of $I_0 = 0.1$ W/cm^2 is used to probe the birefringence changes. It propagates through the crystal coaxially to the intense pump beam, but can be moved relative to it. Right in front of the crystal, the probe beam is polarized linearly at 45° with respect to the optical (z-) axis of the crystal with the help of a polarizer. After propagation through the birefringent material, this linear polarization has changed to an elliptical polarization. A $\lambda/4$-wave plate oriented with its optical axis parallel to the polarizer turns the elliptical polarization back into linear polarization. The corresponding polarization angle is determined with a second polarizer, the so-called analyzer, which is mounted in a rotation stage: rotating this analyzer before and after illumination

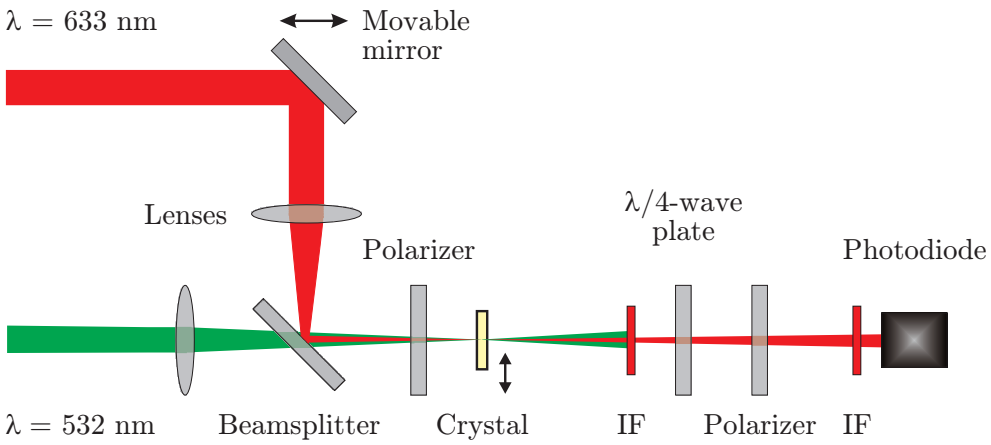

Figure 5.2: Experimental setup for the measurement of light-induced birefringence changes. An intense green pump beam is used to generate the changes. The weak red beam probes them using a phase compensation technique. In order to detect only the signal of the red probe beam, two interference filters (IF) for $\lambda = 633$ nm are used to block the pump beam.

with the intense pump beam gives two sinusoidal intensity modulations, which are recorded with a photodiode. The relative phase between these two modulations $\Delta\phi$ is directly related to the light-induced birefringence changes δn:

$$\Delta\phi = \frac{2\pi d}{\lambda}\delta n \; . \tag{5.4}$$

Here, d is the crystal thickness and λ is the wavelength of the probe light. The method allows the determination of birefringence changes as small as 10^{-6} for our crystal thicknesses $d \approx 0.1 - 1$ mm. The sample is mounted on a translation stage. Therefore, the birefringence changes can be measured at different positions of the crystal.

Chapter 6

Cleaning of iron-doped lithium niobate crystals

Now we proceed to the results obtained for optical cleaning of iron-doped $LiNbO_3$ crystals. First, experiments using coherent laser light are presented. Then, proof-of-principle experiments demonstrating optical cleaning with incoherent light supplied by high-power LED's are shown.

At first sight, optical cleaning of intentionally iron-doped crystals seems contradictory: for a reliable suppression of optical damage, a very low concentration of photoexcitable electrons has to be achieved. In Chapter 3, this concentration has been estimated to be $N_e^{min} \leq 10^{12}$ cm^{-3}. Thus, starting from nominally-undoped material, which contains already one to two orders of magnitude less photoexcitable electrons seems favorable. However, only the iron-doped crystals allow inspection of the achieved cleaning using absorption measurements. Therefore, only doped crystals allow a direct comparison of the experimentally-achieved cleaning with our theoretical predictions on the reduction of photoexcitable electrons.

6.1 The crystals

All iron-doped samples used within this thesis are congruently-melting $LiNbO_3$ crystals from *Deltronic*, which are grown by adding different amounts of Fe_2O_3 to the melt. The distribution coefficient of iron in $LiNbO_3$ at our doping levels is nearly one, i.e. the iron concentrations in the melt and in the crystals can be assumed to be identical.

In Table 6.1, the key figures for our doped $LiNbO_3$ crystals are summarized: the total concentration of iron c_{Fe} is calculated from the production specifications. In our case with only one dopant, c_{Fe} equals the to-

tal concentration of deep charge centers N_e^{Σ}. The concentration of Fe^{2+}, which can be taken as the total concentration of photoexcitable electrons N_e^0, is determined with the help of absorption measurements using a photospectrometer. Equation (5.1) allows to extract the concentration $c_{Fe^{2+}}$ for a given absorption at 477 nm [45]. The same method together with Eq. (5.2) is used to obtain the concentration of H^+ ions, which represent the ionic compensation charges [81].

Crystal label	$x \times y \times z$ [mm^3]	$c_{Fe} = N_e^{\Sigma}$ [10^{17} cm^{-3}]	$c_{Fe^{2+}} = N_e^0$ [10^{17} cm^{-3}]	$c_{H^+} = N_i^0$ [10^{17} cm^{-3}]
DT10-2_2	$1 \times 4 \times 5$	36	0.8	21
DT10-2_3	$1 \times 4 \times 5$	36	0.8	21
DT10-2_4	$1 \times 4 \times 5$	36	0.8	21
DT10-2_5	$1 \times 4 \times 5$	36	0.8	21
DT10-1_2z	$3.5 \times 5 \times 2$	54	3.5	27
DT7-5_6	$1 \times 4 \times 5$	108	4.3	19
DT LED_2	$1 \times 4 \times 5$	180	11	18

Table 6.1: Table of the iron-doped $LiNbO_3$ samples, which are subjected to an optical cleaning treatment.

6.2 Cleaning with a static light pattern

Likewise to the theoretical description of the optical cleaning in Chapter 3, we also proceed from the simplest to more complex cleaning scenarios in this experimental part. Thus, we start with cleaning experiments using a static light pattern. If not specified differently, all the cleaning experiments presented hereafter are performed at a temperature of 180 °C.

Long-time measurement

A long-time measurement allows to estimate the characteristic times needed for a considerable reduction of photoexcitable electrons in the cleaned region. It also gives information about the evolution of the concentration profile of these photoexcitable electrons along the z-axis.

The crystal used for this experiment is DT10-2_2. The parameters of the cleaning light pattern are as follows: a Gaussian-shaped beam with a 1/e-radius of 70 µm and a peak intensity of 1100 W/cm^2 illuminates the crystal in x-direction. After different cleaning times the cleaning process is

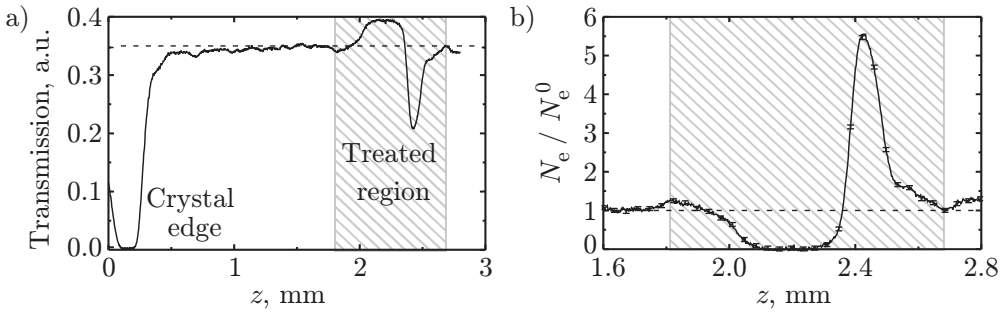

Figure 6.1: a) Transmission profile for the crystal DT10-2_2 after 24 h of static optical cleaning with $I_0 \simeq 1100$ W/cm^2. The dotted line is the mean transmission for the untreated region. b) Normalized concentration N_e/N_e^0 calculated from the transmission profile in Fig 6.1a. The relative concentration $N_e/N_e^0 = 1$ is marked with a dotted line.

interrupted for inspection of the concentration profile $N_e(z)$ by a spatially-resolved absorption measurement (see Section 5.1) using a weak HeNe laser. The advantage of using the HeNe laser is that this measurement can be performed without removing the sample from the cleaning setup. Thus, a precise reconstitution of the previous cleaning position is possible for continuation of the cleaning.

Figure 6.1a shows a typical transmission profile obtained from the absorption measurement after optical cleaning, which is then converted into a profile for the relative concentration of photoexcitable electrons (Fig. 6.1b). In Fig. 6.2, the evolution of such a concentration profile is shown for increasing cleaning times t. Several features are worth mentioning: the region which has been subjected to the optical cleaning treatment can be clearly identified. As it is expected from theory, two distinct regions form: a cleaned one with a concentration of electrons N_e smaller than the initial value N_e^0 and, relative to this region in $+z$-direction, a polluted area, where electrons agglomerate. Longer cleaning times lead to a strongly asymmetric profile with a large cleaned region and a relatively sharp polluted region. In the cleaned region, the concentration of photoexcitable electrons shrinks below the resolution limit for the absorptive detection method already after 6 h of cleaning. The detection limit is in this case about $5 - 10$ % of the initial value N_e^0.

Up to now, only the results of absorption measurements in the crystal DT10-2_2 have been shown. It remains unclear, however, if the observed reduction of photoexcitable electrons actually changes the crystal's behavior with respect to optical damage. Therefor, the same sample is investigated using beam distortion measurements: for different positions along

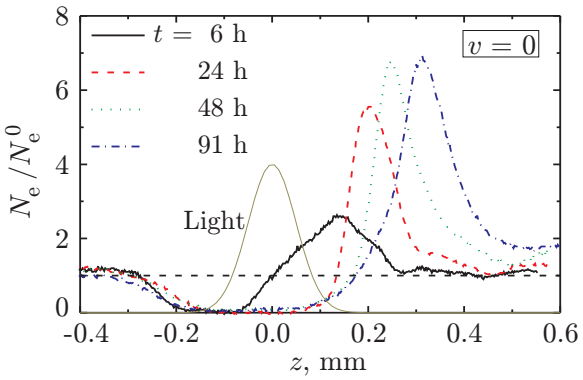

Figure 6.2: Evolution of the normalized concentration profile $N_e(z,t)/N_e^0$ of the crystal DT10-2_2 for increasing cleaning time t. The illuminating beam with a maximum intensity $I_0 = 1100$ W/cm^2 and a 1/e-radius of 70 µm is indicated by the solid, dark yellow line centered around $z = 0$. It is obvious that, with increasing cleaning time, the cleaned region becomes wider. The polluted region, which lies in $+z$-direction with respect to the cleaned area, stays relatively narrow.

the z-axis of the crystal, the threshold intensity I_{Thr} for optical damage is determined. The procedure for the extraction of the threshold from the experimental data is explained in Fig. 6.3. Figure 6.4 shows the profile $I_{Thr}(z)$: an increase of the optical damage threshold by two orders of magnitude is found in the cleaned crystal region.

Intensity dependence

The theoretical considerations have revealed that it is generally favorable to have small dimensionless parameters a, b, c, and $\hat{E}_D$. Whereas it is not difficult to realize experimental cleaning conditions such that the last three parameters fulfill this requirement, $a \ll 1$ is a challenge: taking the standard crystal parameters from Table 3.1, the long-time measurement from the previous section is performed with $a \simeq 67$, $b \simeq 0.04$, $c \simeq 0.02$, and $\hat{E}_D \simeq 0.001$. The easiest way to decrease a experimentally is by reducing the light intensity I_0, although this leads to an increasing characteristic cleaning time t_0. With the following experiment we want to probe the model prediction that such a decrease of a at the expense of t_0 by reducing the intensity I_0 is inferior to the situation with small t_0 and large a.

Therefor, the crystals DT10-2_2, DT10-2_3 and DT10-2_4 are subjected to cleaning treatments with the same experimental parameters as in the long-time measurement, except that smaller light intensities $I_0 = 110$, 11,

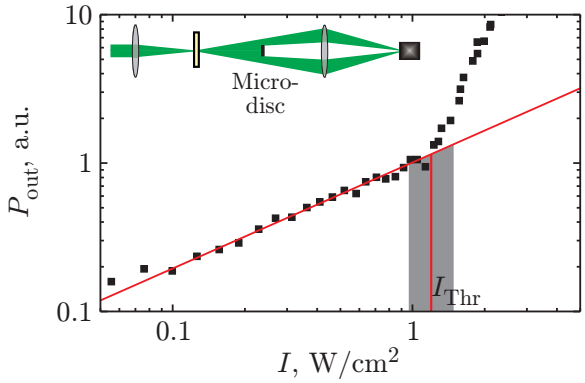

Figure 6.3: Typical data set obtained from the beam distortion measurement described in section 5.2: the power P_{out} of the light passing the micro-disc is given for increasing input intensity I (black dots). The onset of optical damage is attributed to the strong superlinear rise of P_{out}, in this case at about 1.2 W/cm^2. Thus, the corresponding intensity is taken as the threshold intensity for optical damage I_{Thr}. The red lines serve as a guide to the eye for the extraction procedure. The grey-shaded area represents the uncertainty of I_{Thr} for this extraction method, which is about 20 %.

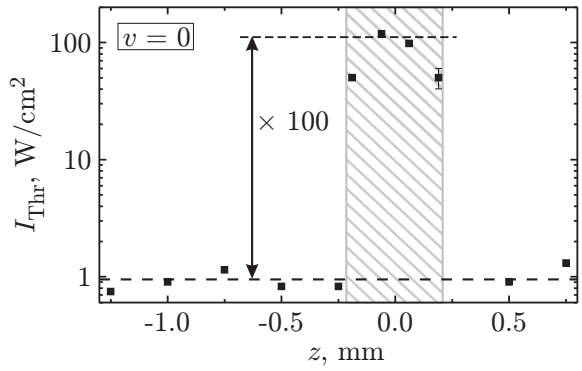

Figure 6.4: Profile of the optical damage threshold for the crystal DT10-2_2 after the long-time optical cleaning treatment with a static beam. The cleaned crystal region is denoted by the hatching.

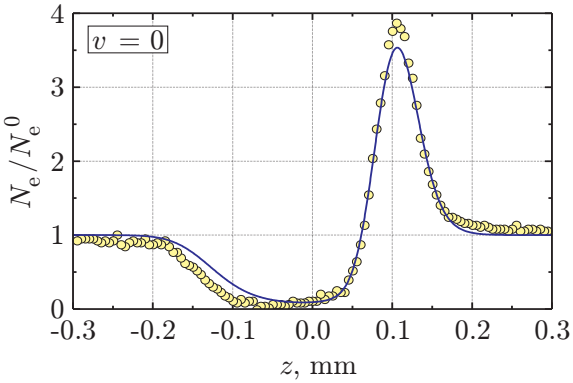

Figure 6.5: Normalized concentration profile $N_e(z,t)/N_e^0$ of the crystal DT10-2_3 after static cleaning for $t = 24$ h with an intensity $I_0 = 11$ W/cm^2 (yellow symbols). The size of the symbols represents the height of the error bars. The dimensionless cleaning parameters are $a = 0.67$, $b \simeq 0.04$, $c \simeq 0.02$, and $\hat{E}_D \simeq 0.001$. The blue line is the result of our numerical simulation for this set of parameters.

and 1 W/cm^2 are used. Thus, the parameter a varies in total from 67 down to 0.067. The characteristic cleaning time t_0 takes on values from 224 sec to 224000 sec = 62 h. An exemplary result of a consecutive absorption measurement performed with the crystal DT10-2_3 is shown in Fig. 6.5. Figure 6.6 gives the minimum normalized concentration N_e^{min}/N_e^0 for the different intensities after different cleaning times t, which are extracted from the absorption measurements. It is obvious that decreasing the intensity in order to reduce a does not improve the optical cleaning with a static light pattern, but gives much worse results after a given time t.

Other ways of experimentally lowering a, e.g., by enriching the crystals with hydrogen or by increasing the temperature are not conducted for the doped samples. The annealing procedure, which is necessary to blow up the hydrogen concentration gives varying results for each crystal, it also affects the oxidization state of the crystal. Thus, too many parameters are changed. Increasing the temperature is not favorable either because thermal excitation of electrons might set in and reduce the cleaning efficiency.

6.3 Cleaning with a moving light pattern

The experiments on the optical cleaning of doped $LiNbO_3$ crystals with a static light pattern have already shown a considerable improvement of the crystals with respect to the optical damage threshold. According to the

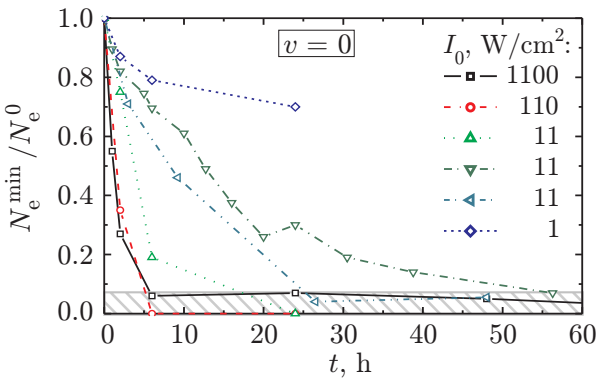

Figure 6.6: Minimum normalized concentration of photoexcitable electrons N_e^{min}/N_e^0 for different light intensities I_0 after different cleaning times t. The hatched area marks the resolution limit for the absorptive detection method. The measurement error on all the points can be estimated as $5-10$ %.

model, the performance of a moving light beam should be even better. In addition, the cleaned regions should become wider. Therefore, this section is dedicated to experiments with moving light beams.

The crystal DT10-2_5 is cleaned for 340 h using a Gaussian-shaped beam with a maximum intensity $I_0 = 15$ W/cm^2 and a 1/e-radius $z_0 = 22$ µm. During the cleaning procedure the crystal is moved for 1 mm in $-z$-direction with the help of a translation stage. In terms of the model this corresponds to values for the dimensionless parameters of $a \simeq 0.9$, $b \simeq 0.04$, $c \simeq 0.02$, $\hat{E}_D \simeq 0.004$, and $v/v_0 \simeq 0.1$. After the optical cleaning, an absorption scan is taken, see Fig. 6.7. It reveals a cleaned crystal region of 1 mm width, where the concentration of photoexcitable electrons has dropped below the detection limit. The polluted area has not widened compared to the experiments using static light patterns. It exhibits a strongly increased concentration of filled charge centers, $N_e/N_e^0 \approx 13$. Note that the convolution of the real concentration profile and the probe beam shape strongly reduces the height and increases the width of the concentration profile in the polluted region.

Figure 6.7 also shows the results of beam distortion measurements using the same crystal. The threshold intensity for optical damage, again determined via the intensity dependence of P_{out}, is increased by more than three orders of magnitude in the optically-cleaned region compared to that of untreated crystal parts.

Additionally, the performance of the optical cleaning of the crystal DT10-2_5 is investigated with the help of birefringence measurements. The re-

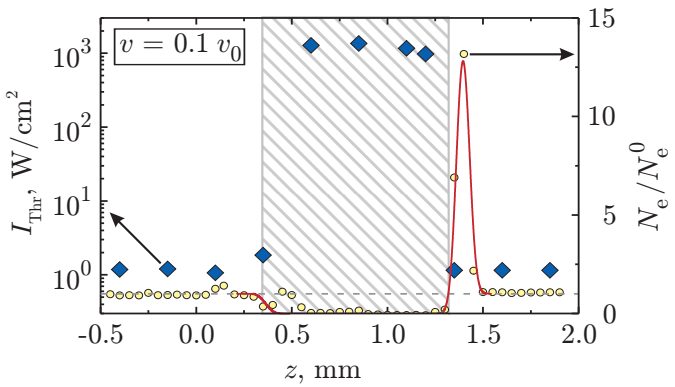

Figure 6.7: Optical damage and absorption behavior of the crystal DT10-2_5 after optical cleaning with a moving beam. The threshold intensity for optical damage I_{Thr} (diamonds, left scale) versus the z-coordinate is shown along with the normalized concentration of photoexcitable electrons $N_{\mathrm{e}}/N_{\mathrm{e}}^0$ (open dots, right scale). The sizes of the symbols reflect the error bars. The continuous line is the result of our numerical simulation. Except for some artefact at the left edge, no absorption is detectable in the optically-cleaned region (hatching) within the resolution limit.

sults are depicted in Fig. 6.8: subfigure a) shows the data obtained for the untreated crystal part, subfigure b) those for the cleaned region. In both cases, the Gaussian shape of the laser beam inducing the birefringence changes is clearly seen. In the uncleaned crystal region, the left part of the birefringence profile shows some broadening. However, the maximum birefringence changes are still well-resolved. Even though more than ten times higher intensities have been used to induce the birefringence changes in the cleaned region, the maximum values are still more than one order of magnitude lower than those in the untreated region.

Breaking of the concentration profile

For $v > v_0$ and, in the case of $a > 1$ for even smaller velocities, the model for the optical cleaning predicts a breaking of the concentration profile $N_{\mathrm{e}}(z)/N_{\mathrm{e}}^0$: the concentration peak, i.e. the polluted region of the crystal, is split from the cleaned region and moves away from it. From this time on, no further cleaning takes place. This behavior is also observed in the following experiment: the crystal DT10-1_2z is cleaned for 77 h using a light beam with $I_0 = 1000$ W/cm^2 and a 1/e-radius $z_0 = 70$ µm, which is moving with a speed of 5 nm/s. After the treatment, an absorption profile is

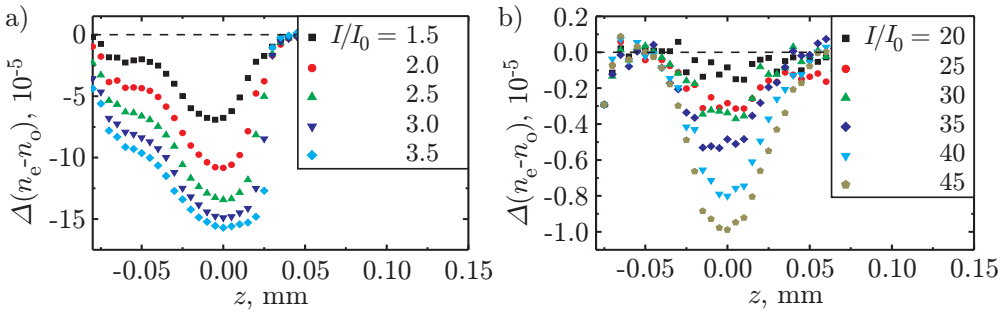

Figure 6.8: Measurement of the birefringence changes $\delta n = (\Delta n_e - \Delta n_o)$ for the crystal DT10-2_5 after optical cleaning with a moving light beam. Graph a) shows the changes for increasing intensities I/I_0 in the uncleaned part of the crystal, graph b) those for the cleaned region.

recorded with the HeNe laser. The corresponding normalized concentration profile is shown in Fig. 6.9: the cleaned crystal region, which is about 0.8 mm wide, is clearly separated from the polluted one. Between the two regions, the concentration of photoexcitable electrons almost returns to the initial value N_e^0. The minimum concentration, which is obtained for the cleaned region, is at the detection limit.

A second optical cleaning treatment with a moving beam starting in the already cleaned region is able to remove the "shoulder", which is observed after the first cleaning (see Fig. 6.10). The cleaned region now extends over more than 1.2 mm. The cleaning parameters for this second cleaning run are: $I_0 = 1000\ \mathrm{W/cm^2}$, $z_0 = 70\ \mu\mathrm{m}$, $v = 4\ \mathrm{nm/s}$, and $t = 72\ \mathrm{h}$.

6.4 Cleaning with incoherent light

As it has already been mentioned in the introduction of this chapter, there are no requirements on the spatial or the temporal coherence of the cleaning light. Consequently, any light source providing suitable wavelengths and intensity levels can be used. In this section, proof-of-principle experiments of the optical cleaning with incoherent light supplied by commercially-available high-power LED's are presented.

A first cleaning attempt with incoherent light is undertaken with a Luxeon V Star 5 W LED incorporated into the setup shown in Fig. 4.4a. The optical output power of the LED is 570 mW at a central wavelength of 505 nm. The crystal DT7-5_6 is cleaned for 140 h using a static light pattern. The result of a successive absorption measurement is shown in Fig. 6.11.

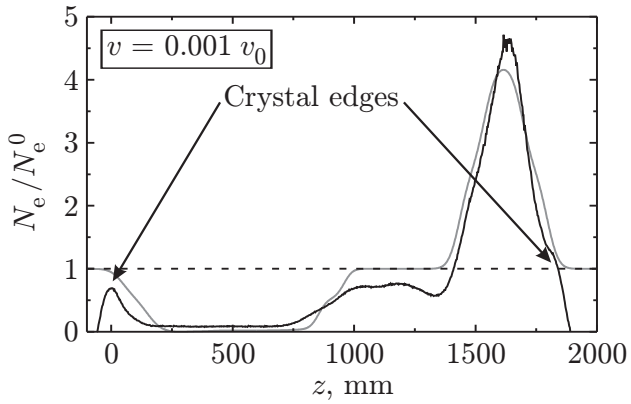

Figure 6.9: Normalized concentration profile $N_e(z)/N_e^0$ of the crystal DT10-1_2z after cleaning with a moving light pattern (black line). For the experimental parameters used, which comply with $a \simeq 192$, $b \simeq 0.13$, $c \simeq 0.065$, $\hat{E}_D \simeq 0.001$, and $v/v_0 = 0.001$, the profile breaks: the polluted region moves away from the cleaned region. In between, the concentration goes back almost to the initial value N_e^0. The grey line is the result of a numerical simulation using the above values for the dimensionless parameters.

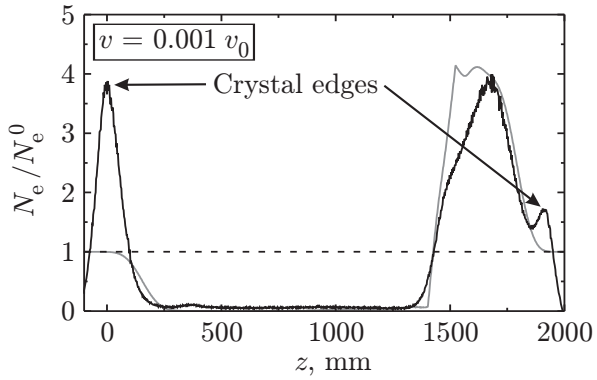

Figure 6.10: Normalized concentration profile $N_e(z)/N_e^0$ for the crystal DT10-1_2z after the second optical cleaning treatment with a moving light pattern (black line). Over the whole cleaned region, which is now approximately 1.2 mm wide, the absorption is below the detection limit. The "shoulder" from Fig. 6.9, where the concentration returns almost to the initial value, has vanished. The result of a numerical simulation starting from the concentration profile $N_e(z)/N_e^0$ given by the grey line in Fig. 6.9 is also shown (grey line).

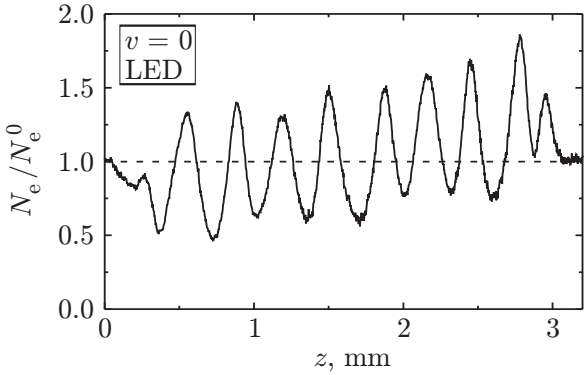

Figure 6.11: Normalized concentration profile $N_e(z)/N_e^0$ for the crystal DT7-5_6 after static optical cleaning with incoherent LED light. The modulation reflects the emitter structure of the Luxeon V Star 5 W LED, which is shown in Fig. 6.12.

The modulation of the concentration of photoexcitable electrons N_e/N_e^0 resembles the light emitting structure of the LED. A picture of this structure is shown in Fig. 6.12. Furthermore, the absorption measurement reveals a slightly increasing concentration N_e/N_e^0 in $+z$-direction. This is most probably due to the imaging of the LED emitter structure onto the crystal, leading to non-zero light intensities between the emitter areas and, thus, to a redistribution of electrons from the $-z$- to the $+z$-side of the illuminated region. The overall cleaning efficiency is not very high: the reduction of N_e/N_e^0 does not exceed 50 %.

A second cleaning attempt with incoherent light is performed with a moving light pattern. Therefor, the crystal DT-LED_2 is moved for 2 mm relative to the cleaning beam in 24 h. This procedure is repeated five times. The starting position along the z-axis for each run is shifted a little bit in $+z$-direction. The incoherent light source is a Luxeon III Star 3 W LED with an optical output power of 450 mW at a central wavelength of 470 nm. Its light emitting area contains only one of the four segments of the Luxeon V Star 5 W LED (see Fig. 6.12). The setup used for the cleaning is sketched in Fig. 4.4b, i.e. the LED is placed right in front of the crystal without any optics. This corresponds roughly to an illuminating light intensity of 10 W/cm^2.

Figure 6.11 shows the results of an absorption measurement using the photospectrometer, which is performed after the last cleaning run. In addition to the normalized concentration $N_e(z)/N_e^0$ of photoexcitable electrons also the concentration profile of H^+ ions is given. It shows very good agreement with the electronic modulation.

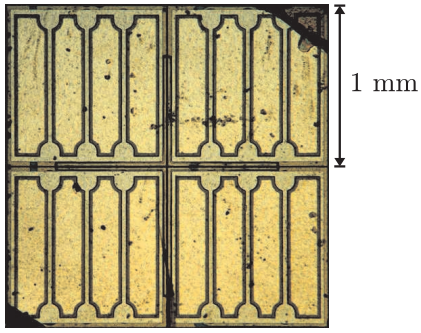

Figure 6.12: Picture of the emitting area of the Luxeon V Star 5 W LED. There are four segments with in total 16 areas, which actually emit light. Each of these areas is approx. 0.2 mm wide and 0.9 mm long. The Luxeon III Star 3 W LED, which is also used in some experiments, contains only one of the four segments.

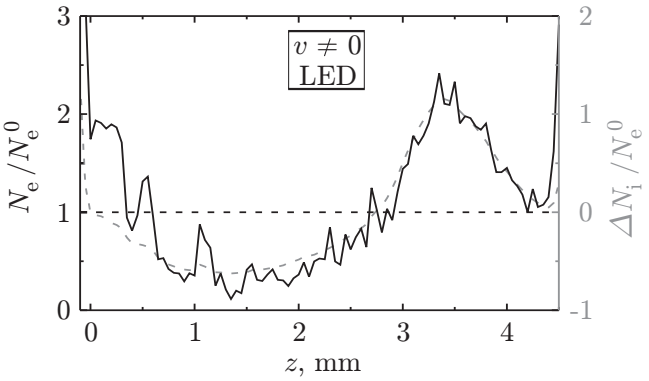

Figure 6.13: Normalized concentration profile $N_e(z)/N_e^0$ for the crystal DT-LED_2 after optical cleaning with a moving pattern of incoherent LED light (black line). The dotted grey line shows the measured H^+ concentration; the concentration change ΔN_i is normalized to the initial concentration of photoexcitable electrons N_e^0.

Chapter 7

Cleaning of nominally-undoped lithium niobate crystals

In chapter 6 it is shown that optical cleaning works in congruently-melting $LiNbO_3$ crystals, which are moderately doped with iron. In the end, however, optical cleaning shall be applied to nominally-undoped, congruently-melting $LiNbO_3$ crystals. Experiments using such crystals are presented in this chapter.

The transition from doped to undoped material is non-trivial: first, the impurity concentrations causing photorefraction in $LiNbO_3$ are much lower in such crystals, on the order of ppm. Hence, these crystals do not allow the application of absorption measurements for tracing and quantifying the optical cleaning. Instead, we have to rely on indirect methods, e.g., measurements of beam distortion or measurements of light-induced birefringence changes.

Second, the charge transport properties are less thoroughly investigated and understood. In a first approximation, we take the cleaning model based on the one-center model and adapt it to cleaning of undoped crystals. Then, we try to optimize the parameters to give efficient cleaning of undoped samples.

In addition, the cleaning time should stay at a reasonable value, i.e. it should not exceed some days. Cleaning a considerable crystal volume in this time span leaves no alternative but to clean with a moving light beam.

7.1 The crystals

The samples utilized are nominally-undoped, congruent $LiNbO_3$ crystals supplied by *Crystal Technology, Inc.* (Crystal Tech). They are grown using

the Czochralski technique. According to mass spectroscopic analyses performed by Crystal Tech, the crystals contain impurities on the order of ppm. An excerpt of such an analysis is given in Table 7.1. Among other elements, several types of impurities causing photorefraction in $LiNbO_3$ are present. The most prominent among them, also with the highest concentration, is iron. Thus, assuming that the one-center model is still applicable and can be used to model optical cleaning seems to be justified.

Element	Concentration [ppm]	Concentration [$10^{16}/cm^3$]
Na	3.5	6.7
Mg	0.5	0.9
Al	1.1	2.1
Ti	0.2	0.4
Cr	**0.9**	**1.7**
Mn	**0.1**	**0.2**
Fe	**1.9**	**3.5**
Cu	**0.4**	**0.8**
Ag	< 1.4	< 2.6

Table 7.1: Excerpt of a mass spectroscopic analysis of nominally-undoped, congruently-melting $LiNbO_3$, performed by Crystal Tech. The elements are given in the order of increasing atomic number. Impurities, which are known to cause photorefraction in $LiNbO_3$, are typed in bold face.

Table 7.2 gives an overview of the used crystals. The concentration of deep traps, which are predominantly iron atoms according to the mass spectroscopic analysis from Table 7.1, is estimated as $N_e^{\Sigma} \approx (0.1 - 1) \times 10^{17}$ cm^{-3}. The concentration of photoexcitable electrons and compensating ions are determined with the help of absorption measurements: whereas the compensating ions are present with large concentrations of $N_i^0 \approx (10 - 100) \times 10^{17}$ cm^{-3} giving a strong absorption signal, the concentration of photoexcitable electrons is too small to be measured. There, we can only estimate an upper limit of $N_e^0 \leq 0.1 \times 10^{17}$ cm^{-3}.

7.2 Cleaning with a moving light pattern

The best cleaning attempt with a moving light beam of Gaussian shape in nominally-undoped $LiNbO_3$ is realized with the crystal W54-26. It is exposed to a Gaussian beam with $I_0 = 1000$ W/cm^2 and $z_0 = 18$ µm for 39 h

Crystal label	$x \times y \times z$ [mm^3]	$c_{\mathrm{Fe}} \simeq N_{\mathrm{e}}^{\Sigma}$ [10^{17} cm^{-3}]	$c_{\mathrm{Fe}^{2+}} \simeq N_{\mathrm{e}}^{0}$ [10^{17} cm^{-3}]	$c_{\mathrm{H}^{+}} = N_{\mathrm{i}}^{0}$ [10^{17} cm^{-3}]
LN-B, LN-C	$1 \times 5 \times 6$	$\approx 0.1 - 1$	≤ 0.1	110
LN-F, LN-G	$1 \times 5 \times 6$	$\approx 0.1 - 1$	≤ 0.1	23
W54-24 – W54-36	$1 \times 5 \times 6$	$\approx 0.1 - 1$	≤ 0.1	15
W54-39	$1 \times 5 \times 6$	$\approx 0.1 - 1$	≤ 0.1	90
W54-50 – W54-54	$1 \times 5 \times 6$	$\approx 0.1 - 1$	≤ 0.1	15

Table 7.2: Table of the nominally-undoped $LiNbO_3$ crystals, which are used for optical cleaning.

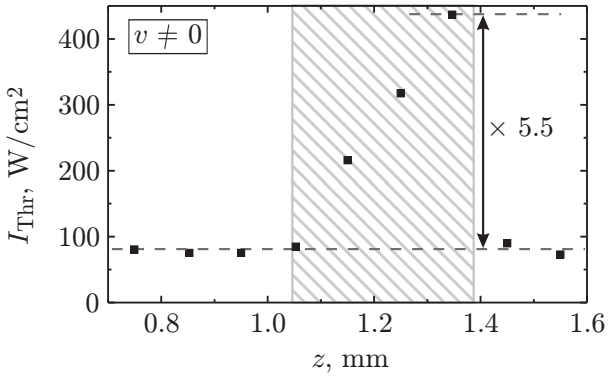

Figure 7.1: Scan of the threshold intensity I_{Thr} along the z-axis for optical damage in the nominally-undoped crystal W54-26 after optical cleaning with a moving beam. In the cleaned region (hatching), the optical damage threshold is increased at maximum by a factor 5.5 with respect to the threshold of untreated crystal parts.

at a temperature of 180 °C. During this treatment, the sample is moved with a velocity $v = 200$ µm/day in $-z$-direction. Afterwards, a scan of the beam distortion behavior along the z-axis is recorded, see Fig. 7.1. The cleaned area is well-identifiable. It exhibits an increasing optical damage threshold from the $-z$-edge to the $+z$-edge. A maximum enhancement factor of $\chi = 5.5$ is observed between the threshold intensities for the cleaned and the untreated crystal parts. The distance of 100 µm between two datapoints is necessary in order to prevent the locally-generated index profiles from overlapping.

In order to prove that an enhancement factor of approx. five can really be extracted reliably from the beam distortion measurements, two sets of raw data from a distortion measurement, one for the cleaned crystal region and one for an untreated region, are given in Fig. 7.2: it is obvious that

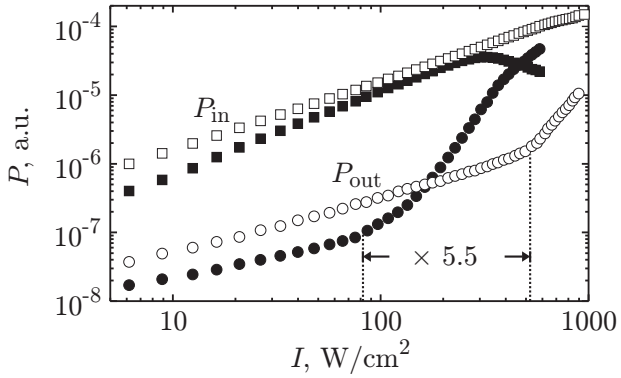

Figure 7.2: Comparison of beam distortion measurements, one of which is performed in the cleaned region of crystal W54-26 (open symbols), the other one in an untreated region (full symbols). Both types of measurements are shown, the one recording P_{in} and the one recording P_{out}. From P_{out}, which shows a more pronounced signal change for the onset of optical damage, the threshold intensities are determined: they differ by a factor 5.5 for cleaned and untreated crystal regions.

the curves are clearly distinguishable, and that even factors considerably smaller than five can be determined.

The sample W54-26 is also investigated with respect to light-induced birefringence changes. The result is shown in Fig. 7.3 in terms of the changes of the ordinary index of refraction Δn_{o}. These changes are diminished by approx. 55 % in the cleaned region. A substructure as it is seen in Fig. 7.1 for the cleaned region does not appear.

Many other cleaning attempts performed with varying parameters I, z_0, v, and T do not lead to an enhanced cleaning efficiency. It is worth mentioning that cleaning experiments under the same conditions lead to roughly the same cleaning results, i.e. they are reproducible. Figure 7.4 shows the results of several treatments for a fixed temperature of 180 °C, characterized by the enhancement χ of the threshold intensity for optical damage. Even though the different parameter sets lead to considerably different cleaning efficiencies, there is no clear trend for which parameter set the theoretically expected dramatic cleaning enhancement may set in.

Table 7.3 gives the cleaning parameters and the obtained enhancement factors χ for a larger excerpt of the cleaning experiments in nominally-undoped crystals. Some of the experiments feature special circumstances not mentioned in the table: the crystals LN–B – LN–G and W54–39 have been subjected to proton enrichment treatments prior to the optical clean-

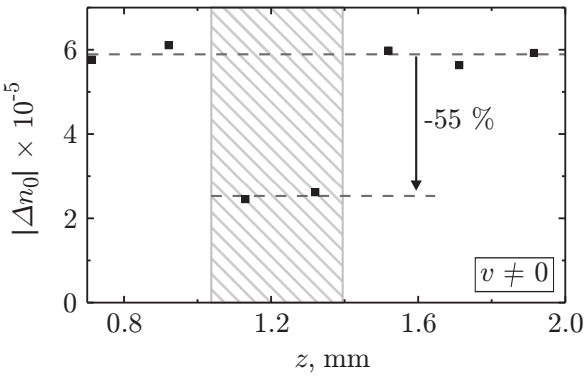

Figure 7.3: Absolute values of the light-induced refractive index changes for ordinarily-polarized light $|\Delta n_o|$ versus position along the z-axis of crystal W54-26. In the cleaned crystal region (hatched area), the index changes are reduced by more than 50 % with respect to those in untreated regions.

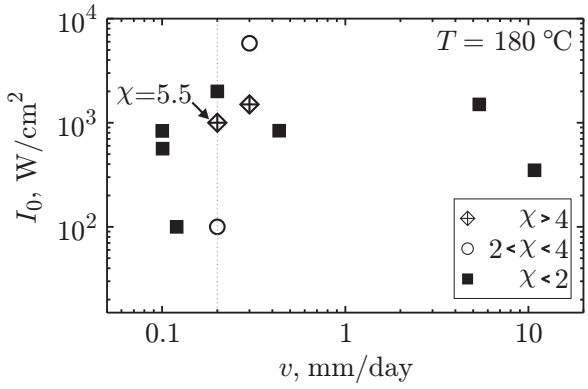

Figure 7.4: Enhancement factor χ versus peak intensity of the Gaussian cleaning beam I_0 and moving velocity of the light beam v. The best cleaning with an enhancement factor of 5.5 is obtained for $I_0 = 1000$ W/cm^2 and $v = 200$ µm/day.

ing. This treatment involves heating of the crystals to 1000 °C in humid atmosphere. However, the cleaning efficiency does not benefit from this treatment for our experimental parameters.

Crystal	I_0 [W/cm^2]	z_0 [μm]	v [μm/day]	Time [h]	T [°C]	χ
LN–B	890	80	430	111	180	1.5
C	580	100	100	120	180	2
F	2200	30	86	233	170	1
G	830	80	100	194	180	1
W 54–24	100	42	120	60	180	1.8
25	100	42	230	24	180	2.6
26	**1000**	**18**	**200**	**39**	**180**	**5.5**
28	1500	18	300	24	180	5.3
30	5800	21	300	24	180	2.1
31	2000	14	200	39	180	1.7
32	15	47	400	24	200	1
33	15	47	100	24	200	1
34	15	47	1000	24	200	1
35	15	47	4000	24	200	1
36	1500	25	5400	13	180	1
39	350	25	10800	10	180	1

Table 7.3: Enhancement χ of the optical damage threshold for different sets of parameters used to clean nominally-undoped $LiNbO_3$ crystals.

7.3 Cleaning with an asymmetric light pattern

Cleaning of nominally-undoped crystals with a moving Gaussian-shaped cleaning beam has not led to a satisfactory cleaning efficiency. A possible reason can be "redirtying" of the cleaned region, as is has been described in section 3.6. The use of asymmetric light patterns with a steep trailing edge and a smooth leading edge can be a means to inhibit "redirtying".

In order to realize such an asymmetric light pattern experimentally a razor blade is introduced in the closed copper oven through a small slit. It is placed right in front of the sample approximately in the middle of the illuminating laser beam coming from the Nd:YAG laser, which is not focused in this case. The resulting beam profile consists of a smooth Gaussian-shaped leading edge with 1/e-radius $z_1 = 0.85$ mm and a steep

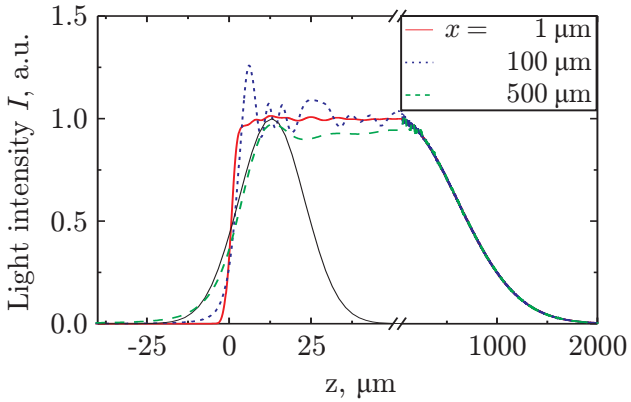

Figure 7.5: Intensity profiles of an initially Gaussian-shaped beam with 1/e-radius $z_1 = 0.85$ mm impinging on an infinite half-plane placed at $z = 0$ for different distances x behind the half-plane. The profiles are calculated taking into account Fresnel diffraction. For comparison with the steep trailing edge of the beam, which is generated experimentally using a razor blade, a Gaussian-shaped light beam with 1/e-radius $z_2 = 14$ µm is also shown (black line).

trailing edge representing a Fresnel-diffracted intensity distribution (see Fig. 7.5). The samples W54–50 – 54 are cleaned with such a light pattern impinging on the x-face, i.e. the crystal thickness in propagation direction is 1 mm. Hence, the trailing edge of the beam does not experience dramatic broadening due to diffraction over the crystal thickness. As it is shown in Fig. 7.5, the width of the trailing edge at the exit face of the crystal is still comparable with a Gaussian-shaped beam with 1/e-radius $z_2 = 14$ µm. The peak light intensity for all experiments with asymmetric beam shape is $I_0 = 115$ W/cm^2, the temperature is $T = 200$ °C. The crystals are moved in $-z$-direction at different velocities in the range of $v = 0 - 100$ µm/day.

Figure 7.6 shows the result of a beam distortion measurement for the best cleaning attempt, which is obtained for a velocity of $v = 10$ µm/day. The threshold intensity for optical damage is increased by roughly one order of magnitude in the cleaned region. The high spatial resolution of the data in the cleaned region is achieved by distributing the data points along the y-axis of the crystal, i.e. perpendicular to the cleaning direction, with a distance of $\Delta y = 100$ µm between two data points. For the other velocities the enhancement χ lies between 3.8 and 5.1. The velocity dependence of χ is shown in Fig. 7.7.

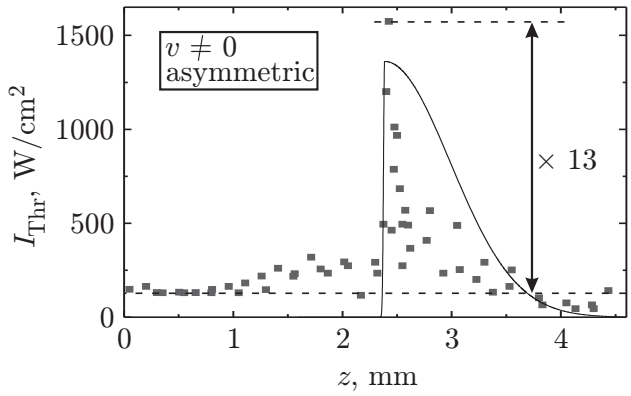

Figure 7.6: Scan of the threshold intensity I_{Thr} for optical damage along the z-axis in the nominally-undoped crystal W54-50 after optical cleaning with a moving, asymmetric light beam as it is shown in Fig. 7.5. Beam profile and position are sketched by the black line. The results are obtained from beam distortion measurements. The optical damage threshold is increased at maximum by a factor $\chi \approx 13$ relative to that of untreated crystal parts.

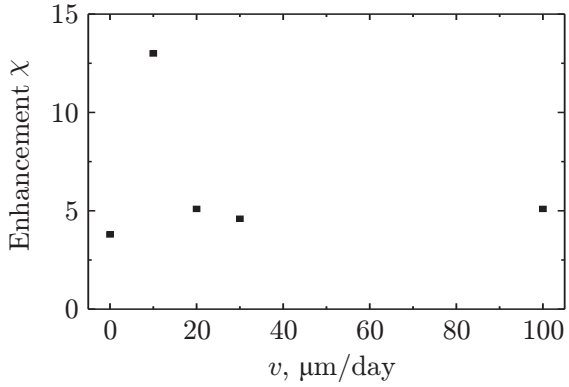

Figure 7.7: Maximum enhancements χ of the optical damage threshold for different velocities v of the cleaning beam for an asymmetric beam shape as it is shown in Fig. 7.5. The error for each data point is approx. 20 %.

Chapter 8

Discussion

In this chapter, first theory and experiment for optical cleaning of iron-doped crystals are compared showing very good agreement for very different cleaning regimes. In order to get an idea of why cleaning has so far not worked well in nominally-undoped crystals the influence of inaccurately known crystal parameters on the cleaning efficiency is investigated. Another possible explanation, namely that the charge transport in undoped crystals is not satisfactorily described by the one-center model, is also discussed. After this, the performance of the optical cleaning method with respect to the optical damage suppression is compared to that of other existing techniques. The chapter is concluded by a short outlook.

8.1 Comparison: measured and computed concentration profiles in iron-doped crystals

A reliable quantitative link between the concentration of photoexcitable electrons and the threshold behavior of optical damage is still missing. The same is true for refractive index changes obtained for high light intensities. Consequently, a quantitative comparison of experimental data on the optical cleaning and our theoretical predictions is limited to iron-doped samples, where it is possible to measure the concentration profiles $N_e(z)/N_e^0$.

Such comparisons are given in Chapter 6 for several cleaning configurations. The theoretical concentration profiles are calculated using the experimental parameters of each cleaning run together with the standard crystal parameters from Table 3.1 and performing a convolution of the profile $N_e(z)/N_e^0$ with the intensity profiles of the probe beams.

The first comparison is given in Fig. 6.5 for static cleaning with a Gaussian-shaped light beam and moderate parameter values ($t = 24$ h $\simeq$ 5.5 t_0, $a \simeq 0.67$, and $b, c, \hat{E}_D \ll 1$). Good agreement between the experimental data and the model simulation is evident. There are only small deviations in the peak region, whose shape is strongly affected by the convolution with the probe beam, and the rear part of the cleaned region. Figure 6.7 shows a comparison of measured and modeled concentration profiles for more challenging cleaning parameters used in conjunction with a moving cleaning beam ($t = 340$ h $\simeq 339$ t_0, $v/v_0 \simeq 0.1$, $a \simeq 0.9$, and $b, c, \hat{E}_D \ll 1$). Even though the absorption measurement cannot resolve the minimum concentration in the cleaned region anymore, the width of this region matches that of the simulation quite well. Moreover, the measurement also shows a strong rise of N_e^{max}/N_e^0 together with a relatively narrow polluted region, just as it is expected from theory and modeled by the numerical simulation. The third, and probably most critical test for our model is the cleaning scenario involving breaking of the profile ($t = 77$ h $\simeq 1609$ t_0, $v/v_0 \simeq 0.01$, $a \simeq 192$, and $b, c, \hat{E}_D \ll 1$). The corresponding comparison between theory and experiment is shown in Figs. 6.9 and 6.10. Again, the measured profiles show good agreement with those of the simulation. The prominent features, e.g., the width of the cleaned region, the point of profile breaking, and shape and height of the polluted region, are in nice agreement.

A further proof for the validity of our model is obtained from Fig. 6.13, where, in addition to the electronic concentration profile, also the concentration profile for the compensating H^+ ions is given. The profiles overlap both, qualitatively and quantitatively. Thus, charge compensation can indeed be attributed entirely to the movement of H^+ ions, as it was expected from Refs. 35 and 75.

Altogether, our model seems to describe the optical cleaning in iron-doped crystals very well. Moreover, our set of standard crystal parameters from Table 3.1 leads to expected cleaning results, which are close to the measured values.

However, the results obtained for the birefringence measurements (Fig. 6.8) leave some open questions: is the concentration of photoexcitable electrons reduced to such an amount that space charge limitation limits the light-induced birefringence changes? In that case we should not observe the increase of the birefringence changes with intensity, unless it were caused by other mechanisms. Such other mechanisms would then limit the increase of the optical damage threshold, which is achievable with the optical cleaning. A second issue are the maximum birefringence changes in the cleaned crystal region, which are observed for the birefrin-

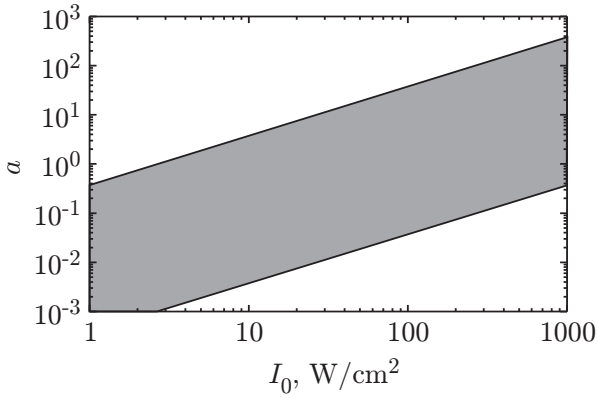

Figure 8.1: Dependence of the dimensionless parameter a on the light intensity I_0 at a temperature of 180 °C in the case of undoped crystals: the grey area depicts the uncertainty of a due to the errors of the crystal parameters (see Chapter 3).

gence measurements: even for the highest intensities they do not exceed 10^{-5}. Since the crystal still shows optical damage in this region, limiting the light-induced birefringence changes to 10^{-5} may be not enough to suppress optical damage, in contrast to our simple estimate at the beginning of chapter 3. Which index changes are tolerable depends on many experimental parameters, in particular on the crystal length.

8.2 Challenges for optical cleaning of nominally-undoped $LiNbO_3$ crystals

The optical cleaning of nominally-undoped samples remains less predictable, as Fig. 7.4 and Table 7.3 have shown. This can be due to several reasons: the photoelectric, thermal, and diffusion related properties of these crystals are known only with poor accuracy (see Chapter 3). Hence, it is possible that the cleaning experiments have been performed under very unfavorable conditions, i.e. bad values for the dimensionless parameters determining the cleaning performance.

Exemplarily, the uncertainty of the cleaning parameter $a = \sigma_{\mathrm{ph}}^0/\sigma_{\mathrm{i}}^0$ is shown in Fig. 8.1. It is obvious that within our examined intensity range, we can have either very favorable (< 0.1) or undesired (> 1) values for a. But not only the parameter a is inaccurately determined, the same is true for the other parameters: since the concentration of photoexcitable electrons N_{e}^0 cannot be measured accurately in undoped samples, it is only

possible to give an upper limit for the parameters b and c. In the case of $b = N_e^0/N_i^0$ this is not dramatic because the concentration of compensating ions N_i^0 in the crystals is definitely much larger than N_e^0, i.e. $b \ll 1$. The situation is more complicated for $c = N_e^0/N_e^{\Sigma}$, where N_e^{Σ} is the total amount of deep charge centers: as it has been mentioned in chapter 3.6, large values of c limit the width of the cleaned area to z_0/c for cleaning with a moving Gaussian-shaped beam. Since, for undoped samples, we cannot definitely exclude large c, i.e. depletion of empty charge centers, this might explain the bad cleaning results.

Furthermore, the exponential cleaning enhancement for cleaning with a moving Gaussian-shaped beam is observed only for moving velocities $0 < v < v_0$ (see Figs. 3.9 and 3.10). In the presence of some experimentally-unavoidable background illumination of intensity I_b, this range shrinks to $(I_b/I_0)\, v_0 < v < (1 + I_b/I_0)\, v_0$ (see chapter 3.7), which can be only one order of magnitude. Finally, the cleaning velocity should be balanced with the value of a to achieve good cleaning and, at the same time, to prevent profile breaking (see Figs. 3.11 and 3.13). Therefore, also accurate knowledge of the photovoltaic drift velocity $v_0 = \beta I/e$ for the undoped crystals is required.

In order to obtain more reliable data for nominally-undoped $LiNbO_3$ crystals, especially on their photoelectric properties, time-resolved birefringence measurements have been conducted [62, 68]. An excerpt of the results obtained in Ref. 62, with which we have tried to optimize the cleaning of undoped crystals, is shown in Fig. 8.2. Unfortunately, the optimization has so far not led to enhanced cleaning efficiencies.

However, the measurements reveal an important feature, which has already been observed earlier [63, 64, 68] and which may cause the bad cleaning results obtained for nominally-undoped crystals: all three determined photoelectric properties, the steady-state space charge field E_{Pv}, the bulk photovoltaic coefficient β, and the photoconductivity σ_{ph}, show intensity dependences, which are not in agreement with the predictions of the one-center model, but with those for a two-center charge transport model [12, 59]. This is true already for relatively small light intensities. Corresponding measurements at $150 - 200$ °C are difficult to perform so that it remains unclear, whether the two-center model is also relevant at the temperatures used for optical cleaning. In any way, the optical cleaning should in principle still work: long-time exposure of a crystal volume should still result in a drastically reduced concentration of photoexcitable electrons in this region.

Nevertheless, certain aspects related to moving cleaning beams have to

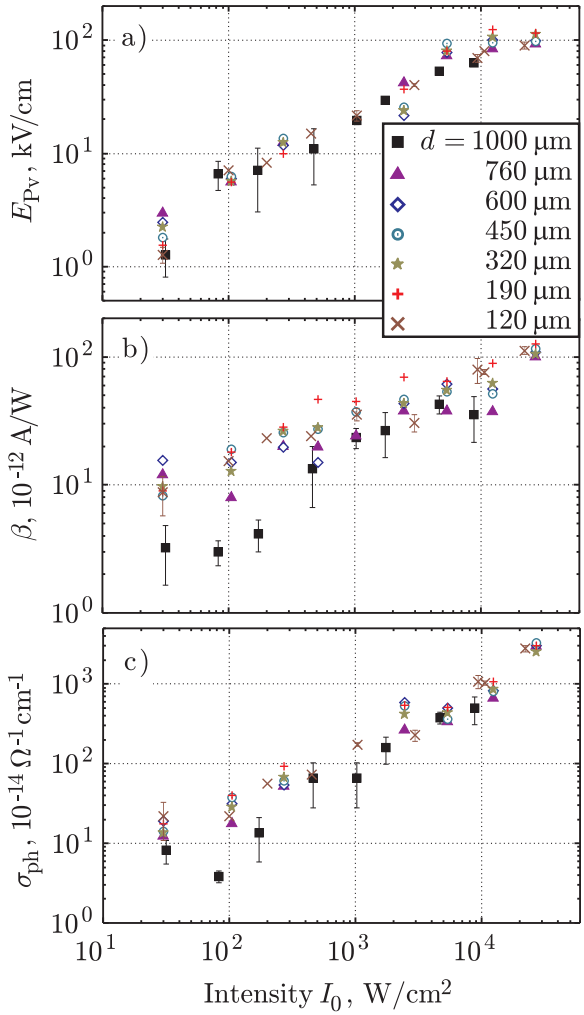

Figure 8.2: Intensity dependences for a) the saturation space charge field E_{Pv}, b) the photovoltaic coefficient β, and c) the photoconductivity σ_{ph} for nominally-undoped, congruently-melting $LiNbO_3$ crystals of different thicknesses d. [62]

be taken into account: the rise of the photovoltaic coefficient with increasing intensity indicates that there is a contribution of the second center to the photovoltaic effect. Moreover, the corresponding bulk photovoltaic coefficient is expected to be higher for the second center. Hence, as soon as the second center plays a significant role for the charge transport, the mean photovoltaic drift velocity v_0 increases and a spectrum of drift velocities forms around this mean velocity. If this spectrum is too broad, for any moving velocity we choose only part of the electrons are subject to optimum cleaning conditions, whereas for others the situation involves supercritical cleaning velocities and bad cleaning efficiencies.

A similar situation is present, when the charge transport related to the second center is given by an undirected hopping movement of the electrons, as it has recently been proposed [82]. In this case, there is also a spectrum of drift velocities around the central velocity v_0. The width of this spectrum depends on the ratio of directed to undirected electronic movements and determines the amount of electrons, which are subject to optimum cleaning conditions and are effectively removed from the exposed region.

Under the circumstances described above for cleaning of nominally-undoped crystals, it seems more advisable to apply asymmetric light beams with a very steep trailing edge. The experiments presented in section 7.3 seem to support this hypothesis, yielding an improvement factor for the optical damage threshold of more than one order of magnitude. Several challenges mentioned above are less important in the case of asymmetric cleaning beams: first, the smooth leading edge of the asymmetric beam broadens the polluted region and weakens the consequences of a depletion of empty charge centers. Together with the more robust behavior concerning large values of a, profile breaking is reduced. Furthermore, the sharp trailing edge strongly reduces the concentration of photoexcitable electrons already for relatively small moving velocities of the beam. That way, the bad influence of different optimum cleaning velocities might be reduced.

However, all efforts to improve the optical cleaning in undoped crystals rely on the assumption that optical damage in these crystals is caused by photoexcitable electrons. If this assumption is not true, the cleaning results obtained for nominally-undoped crystals might already be the best-achievable with this method.

8.3 Optical cleaning versus other crystal refinement methods

In this section, the methods for optical damage suppression in $LiNbO_3$ crystals, which have been introduced in chapter 2, are compared to our optical cleaning method applied to nominally-undoped, congruently-melting crystals.

Before we start this comparison, let us first formulate the goal of the crystal refinement methods: most applications involving second harmonic generation (SHG) in $LiNbO_3$ crystals require output light intensities of the generated light on the order of 100 mW to 1 W. Untreated congruent, nominally-undoped $LiNbO_3$ crystals allow generation of approx. $10 - 50$ mW [34, 83]. Thus, an improvement of $10 - 100$ with respect to the SHG output power of untreated crystals is sufficient to cover the needs of most applications. Since light-induced phase-mismatch, which mainly disturbes SHG generation, and macroscopic beam distortion are correlated, a strong enhancement of the SHG output power is expected if the threshold intensities for beam distortion are enhanced. Beam distortion measurements should, in a rough estimate, provide at least similar improvement factors for the optical damage threshold compared to direct SHG measurements.

In the following, such beam distortion measurements are used to compare the different crystal refinement techniques. For a more comprehensive comparison including achieved green light output powers in SHG experiments the reader is again referred to Ref. 70.

Just like in chapter 2 we start with studies of crystals with an almost stoichiometric composition: little data is available for such crystals, but improvement factors for the optical damage threshold of two compared to untreated material have been measured [19]. This improvement is in no relation with the efforts necessary for the production of such crystals.

Operation of the $LiNbO_3$ crystals at elevated temperatures results in improvement factors of 5 (120 °C) to 30 (200 °C) [30, 84]. These improvement factors are only partly better than those obtained for our optical cleaning. Nevertheless, the elevated temperatures are also the method's biggest disadvantage: stable operation of a nonlinear-optical device at such temperatures is very difficult. Extra care has to be taken with respect to heat diffusion and convection.

With the most successful state-of-the-art technique, doping of congruent $LiNbO_3$ with Mg above a threshold concentration of 5.5 mol%, improvement factors larger than 2000 have been achieved [83]. Even higher

factors of $10^4 - 10^5$ have been realized for Mg-doped VTE treated and near-stoichiometric crystals, respectively [29]. There are two main disadvantages of the Mg-doped crystals compared to congruently-melting crystals: the production of the material is more difficult and costly. Furthermore, periodical poling of the crystals, which is needed for quasi-phase matching, is complicated. At the moment, however, internationally intense efforts are undertaken to overcome these disadvantages. Together with the high suppression factors for optical damage, Mg doping will probably stay the benchmark technique.

In comparison to the sole method from chapter 2, which also attacks the photoexcitable electrons, namely the thermo-electric oxidization, the optical cleaning produces similar suppression factors for optical damage (≈ 10) [33]. The main advantage of the optical cleaning is that it is a very gentle treatment, which can be performed at low temperatures. However, the thermo-electric oxidization can be adapted more easily to large crystal volumes, which is also true for all the other previously-mentioned crystal refinement techniques.

Advantages of the optical cleaning treatment are that congruently-melting $LiNbO_3$ can be used and that the crystals are very robust even after cleaning. The treatment can also be tailored to address photoexcitable electrons trapped at a certain species of deep centers by choosing the right excitation wavelength.

8.4 Outlook

The experimental results presented in this thesis have shown that optical cleaning can indeed modify the electronic structure of lithium niobate crystals. This works particularly well in intentionally iron-doped samples. There, the optical damage resistance is increased by more than three orders of magnitude.

However, cleaning of nominally-undoped congruently-melting crystals, which are most relevant for applications, has not worked as well as it was expected from our theory based on the one-center model. Several reasons for this have been presented.

They encourage further studies: we might just not have used the right set of parameters for the cleaning. Since there are several "screws" to turn, optimization of the cleaning is not a simple task. It can be accomplished by systematically employing a larger range of values for the key parameters.

Another ansatz, which seems more convincing in this context, relies on a more detailed study of a) the formation of optical damage in such crys-

tals and b) the charge transport properties of nominally-undoped crystalline material, especially for high temperatures of $150 - 250$ °C. Measurements at room temperature have shown that the formation of refractive index changes in this material exhibiting a very low concentration of extrinsic defects cannot be described satisfactorily by the one-center model [62, 68].

Once good cleaning, i.e. a strong decrease of the concentration of photoexcitable electrons in a macroscopic region of $0.1 - 1$ mm, is realized also for nominally-undoped $LiNbO_3$ crystals, the next logical step is the application of cleaned material for nonlinear-optical processes, e.g., frequency conversion.

This requires usage of periodically-poled crystals with periodically-arranged domains exhibiting an inverted spontaneous polarization. Two ways of preparing such crystals are possible: either, the crystal is first optically-cleaned and then periodically-poled or the other way round. The former procedure allows the usage of a conventional cleaning scheme, i.e. with a light beam moving only in $+z$-direction. The latter procedure can be applied to a conventionally-poled crystal. In this case, the sign of the bulk photovoltaic coefficient β changes with the orientation of the spontaneous polarization leading to photovoltaic currents in $+z$- and $-z$-direction [40]. Consequently, also the cleaning beam has to be moved in both directions such that first the crystal regions with one domain orientation are cleaned and then the remaining ones.

The possibility to clean a crystal, which is basically ready for application in a device, i.e. which has already been poled and so on, is a great advantage of the optical cleaning technique: poling can be done using regular setups and parameter sets. Furthermore, any degradation of the crystal performance with ongoing operation of the device due to "redirtying" of the cleaned crystal area with photoexcitable electrons can be suppressed at any time by a renewed cleaning treatment.

Finally, the method of optical cleaning is, of course, not restricted to $LiNbO_3$. It can be applied to any non-centrosymmetric crystal showing the bulk photovoltaic effect and a sufficient amount of compensating charge carriers.

Optical cleaning also works just via the diffusion contribution to the electronic current. Thus, any optically transparent material can be subjected to optical cleaning treatments in order to diminish the number of photoexcitable electrons. However, such diffusion-based cleaning requires an intensity pattern with very strong gradients in order to yield considerable diffusion currents. Furthermore, it does not show the exponential cleaning enhancement for moving cleaning beams.

Chapter 9

Summary

Lithium niobate crystals are very attractive for advanced photonics, in particular for nonlinear optics. For many applications, however, photoexcitable electrons trapped at remnant impurities, especially at transition metals like iron, represent a serious threat. They cause optical damage: the formation of unwanted refractive index changes upon illumination of the crystals with intense laser light leading to severe beam distortions.

So far, in nominally-undoped, congruently-melting $LiNbO_3$ crystals improved production techniques have only lowered the concentration of disturbing impurities to several ppm, which is still orders of magnitude too high for an efficient suppression of optical damage. Therefore, other methods for optical damage suppression have been developed. Currently, the most successful approach is doping of the crystals with high concentrations of metal ions like Mg. Nevertheless, each of the methods comes with other drawbacks, in the case of Mg doping complicated production and domain engineering.

In this thesis we investigate a new method for optical damage suppression, the so-called "optical cleaning". It makes use of the bulk photovoltaic effect in $LiNbO_3$: exposure of the crystal leads to a directional electron flow. Simultaneous heating of the crystal to moderate temperatures of 180 °C enables charge compensation by thermally-mobilized, optically-passive ions like H^+. Theoretical considerations of the optical cleaning process in the framework of the known one-center charge transport model lead to very interesting predictions: while usage of a static, Gaussian-shaped light beam already decreases the concentration of photoexcitable electrons, a tremendous enhancement of this effect is expected for moving cleaning beams. At a moving velocity of approx. 0.6 times the photovoltaic drift velocity, a strong exponential decrease of the electron concentration is predicted in the exposed area. Thus, a decrease of the

electron concentration to a level, where optical damage is suppressed due to space charge limitation, should be possible.

The efficiency of the cleaning process is governed mostly by the crystal temperature and the beam parameters intensity, beam radius, and moving velocity. Relevant crystal properties are the electronic and ionic conductivities, the concentration of photoexcitable electrons and that of the ionic compensation charges.

The model is tested experimentally with iron-doped samples, which allow inspection of the achieved cleaning via absorption measurements. The recorded concentration profiles show nice agreement with the model predictions. This is true also in the case of moving cleaning beams and even for parameter sets, which lead to a separation of cleaned and polluted regions. In some cases, the absorption in the cleaned region drops below the resolution limit of the absorption measurements. Subsequent measurements of the optical damage threshold reveal an improvement resulting from optical cleaning of more than three orders of magnitude.

In a next step, the cleaning treatment is applied to nominally-undoped $LiNbO_3$ crystals. The best result is obtained for a slowly-moving, asymmetric light beam with a smooth leading and a steep trailing edge. There, the cleaned region shows an increase of the optical damage threshold by roughly one order of magnitude compared to that of untreated crystal regions.

Nevertheless, especially with respect to the undoped samples, further studies are necessary to improve the cleaning efficiency. Once this has been accomplished, the method becomes very attractive for the refining of $LiNbO_3$ crystals for nonlinear-optical applications. Its great advantage compared to other treatments is that this rather gentle cleaning treatment can be applied to cheap, mass-produced congruently-melting $LiNbO_3$.

Moreover, the optical cleaning can be applied to other piezo- and pyroelectric crystals, which exhibit the bulk photovoltaic effect. In principle, cleaning based solely on diffusion of the electrons is also possible, but requires disproportionately larger cleaning times.

Bibliography

[1] T. H. Maiman, "Stimulated optical radiation in ruby," Nature **187**, 493 (1960).

[2] P. A. Franken, A. E. Hill, C. W. Peters, and G. Weinreich, "Generation of optical harmonics," Phys. Rev. Lett. **7**, 118 (1961).

[3] A. M. Prokhorov and Y. S. Kuz'minov, *Physics and chemistry of crystalline lithium niobate* (Adam Hilger, Bristol and New York, 1990).

[4] Y. S. Kuz'minov, *Lithium niobate crystals* (Cambridge International Science Publishing, 1999).

[5] K.-H. Hellwege, *Landolt Börnstein – Numerical data and functional relationships in science and technology, New series,* **III/16** (Springer Verlag, 1981).

[6] J. Seres, "Dispersion of second-order nonlinear optical coefficient," Appl. Phys. B **73**, 705 (2001).

[7] L. Arizmendi, "Photonic applications of lithium niobate crystals," Phys. Stat. Sol. a **201**, 253 (2004).

[8] M. M. Fejer, G. A. Magel, D. H. Jundt, and R. L. Byer, "Quasi-phase-matched 2nd harmonic-generation - tuning and tolerances," IEEE J. Quant. Elect. **28**, 2631 (1992).

[9] M. Houé and P. Townsend, "An introduction to methods of periodic poling for second-harmonic generation," J. Phys. D **28**, 1747 (1995).

[10] A. Ashkin, G. D. Boyd, J. M. Dziedzic, R. G. Smith, A. A. Ballman, J. J. Levinstein, and K. Nassau, "Optically-induced refractive index inhomogeneties in $LiNbO_3$ and $LiTaO_3$," Appl. Phys. Lett. **9**, 72 (1966).

[11] V. Fridkin and B. Sturman, *The photovoltaic and photorefractive effects in noncentrosymmetric Materials* (Gordon and Breach Science Publishers, 1992).

[12] K. Buse, "Light-induced charge transport processes in photorefractive crystals I: Models and experimental methods," Appl. Phys. B **64**, 273 (1997).

[13] F. S. Chen, J. T. LaMacchia, and D. B. Fraser, "Holographic storage in lithium niobate," Appl. Phys. Lett. **13**, 223 (1968).

[14] H. J. Coufal, D. Psaltis, and G. T. Sincerbox, *Holographic Data Storage* (Springer Berlin, 2000).

[15] S. Breer and K. Buse, "Wavelength demultiplexing with volume phase holograms in photorefractive lithium niobate," Appl. Phys. B **66**, 339 (1998).

[16] S. Breer, H. Vogt, I. Nee, and K. Buse, "Low-crosstalk WDM by Bragg diffraction from thermally fixed reflection holograms in lithium niobate," Electr. Lett. **34**, 2419 (1998).

[17] O. F. Schirmer, O. Thiemann, and M. Wöhlecke, "Electron small polarons and bipolarons in $LiNbO_3$," J. Phys. Condens. Matt. **21**, 123 201 (2009).

[18] G. E. Peterson, A. M. Glass, A. Carneval, and P. M. Bridenbaugh, "Control of laser damage in $LiNbO_3$," J. Am. Ceram. Soc. **56**, 278 (1973).

[19] M. Fontana, K. Chah, M. Aillerie, R. Mouras, and P. Bourson, "Optical damage in undoped $LiNbO_3$ crystals," Opt. Materials **16**, 111 (2001).

[20] Y. Furukawa, M. Sato, K. Kitamura, Y. Yajima, and M. Minakata, "Optical-damage resistance and crystal quality of $LiNbO_3$ single-crystals with various [Li]/[Nb] ratios," J. Appl. Phys. **72**, 3250 (1992).

[21] G. I. Malovichko, V. G. Grachev, E. P. Kokanyan, O. F. Schirmer, K. Betzler, B. Gather, F. Jermann, S. Klauer, U. Schlarb, and M. Wöhlecke, "Characterization of stoichiometric $LiNbO_3$ grown from melts containing K_2O," Appl. Phys. A **56**, 103 (1993).

[22] R. Holman, P. Cressman, and J. Revelli, "Chemical control of optical damage in lithium niobate," Appl. Phys. Lett. **32**, 280 (1978).

[23] D. Jundt, M. Fejer, and R. Byer, "Optical properties of lithium-rich lithium niobate fabricated by vapor transport equilibrium," IEEE J. Quant. Elec. **26**, 135 (1990).

[24] G. G. Zhong, J. Jin, and Z. K. Wu, "Measurements of optically induced refractive-index damage of lithium niobate doped with different concentrations of MgO," J. Opt. Soc. Am. **70**, 631 (1980).

[25] D. A. Bryan, R. Gerson, and H. E. Tomaschke, "Increased optical damage resistance in lithium niobate," Appl. Phys. Lett. **44**, 847 (1984).

[26] Y. Furukawa, K. Kitamura, S. Takekawa, K. Niwa, and H. Hatano, "Stoichiometric Mg:$LiNbO_3$ as an effective material for nonlinear optics," Opt. Lett. **23**, 1892 (1998).

[27] K. Niwa, Y. Furukawa, S. Takekawa, and K. Kitamura, "Growth and characterization of MgO doped near stoichiometric $LiNbO_3$ crystals as a new nonlinear optical material," J. Cryst. Growth **208**, 493 (2000).

[28] L. Palfalvi, G. Almasi, J. Hebling, A. Peter, and K. Polgar, "Measurement of laser-induced refractive index changes of Mg-doped congruent and stoichiometric $LiNbO_3$," Appl. Phys. Lett. **18**, 2245 (2002).

[29] S. S. Chen, H. D. Liu, Y. F. Kong, Z. H. Huang, J. J. Xu, and G. Y. Zhang, "The resistance against optical damage of near-stoichiometric $LiNbO_3$:Mg crystals prepared by vapor transport equilibration," Opt. Materials **29**, 885 (2007).

[30] J. Rams, A. Alcázar-de-Velasco, M. Carrascosa, J. M. Cabrera, and F. Agulló-López, "Optical damage inhibition and thresholding effects in lithium niobate above room temperature," Opt. Commun. **178**, 211 (2000).

[31] Y. Ninomia and T. Motoki, "$LiNbO_3$ light modulator," Rev. Sci. Instr. **43**, 519 (1972).

[32] M. Falk and K. Buse, "Thermo-electric method for nearly complete oxidization of highly iron-doped lithium niobate crystals," Appl. Phys. B **81**, 853 (2005).

[33] M. Falk, T. Woike, and K. Buse, "Reduction of optical damage in lithium niobate crystals by thermo-electric oxidization," Appl. Phys. Lett. **90**, 251 912 (2007).

[34] I. Breunig, M. Falk, B. Knabe, R. Sowade, K. Buse, P. Rabiei, and D. H. Jundt, "Second harmonic generation of 2.6 W green light with thermo-electrically oxidized undoped congruent lithium niobate crystals below 100 °C," Appl. Phys. Lett. **91**, 221 110 (2007).

[35] T. Volk and M. Wöhlecke, "Thermal fixation of the photorefrative holograms recorded in lithium niobate and related crystals," Crit. Rev. Solid State Mater. Sci. **30**, 125 (2005).

[36] J. J. Amodei and D. L. Staebler, "Holographic pattern fixing in electro-optic crystals," Appl. Phys. Lett. **18**, 540 (1971).

[37] A. Becker, ""Thermal fixing" of Ti-indiffused $LiNbO_3$ channel waveguides for reduced photorefractive susceptibility," Appl. Phys. Lett. **45**, 121 (1984).

[38] R. S. Weis and T. K. Gaylord, "Lithium niobate: summary of physical properties and crystal structure," Appl. Phys. **37**, 191 (1985).

[39] M. E. Lines and A. M. Glass, *Principles and applications of ferroelectric and related materials* (Clarendon Press, 1977).

[40] J. F. Nye, *Physical properties of crystals* (Oxford University Press London, 1979).

[41] O. F. Schirmer, O. Thiemann, and M. Wöhlecke, "Defects in $LiNbO_3$ – I. Experimental aspects," J. Phys. Chem. Solids **52**, 185 (1991).

[42] S. C. Abrahams and P. Marsh, "Defect structure dependence on composition in lithium niobate," Acta Crystallogr. Sect. B **42**, 61 (1986).

[43] D. Redfield and W. J. Burke, "Optical absorption edge of $LiNbO_3$," J. Appl. Phys. **45**, 5421 (1974).

[44] E. Krätzig and R. Orlowski, "Light-induced charge transport in doped $LiNbO_3$ and $LiTaO_3$," Ferroelectrics **27**, 241 (1980).

[45] H. Kurz, E. Krätzig, W. Keune, H. Engelmann, U. Gonser, B. Dischler, and A. Räuber, "Photorefrative centers in $LiNbO_3$, studied by optical-, Mössbauer- and EPR-methods," Appl. Phys. **12**, 355 (1977).

[46] I. Nee, M. Müller, K. Buse, and E. Krätzig, "Role of iron in lithium-niobate crystals for the dark-storage time of holograms," J. Appl. Phys. **88**, 4282 (2000).

[47] E. Krätzig and R. Orlowski, "Photorefractive effects and photoconductivity in $LiNbO_3$:Fe," Ferroelectrics **21**, 635 (1978).

[48] R. Orlowski and E. Krätzig, "Holographic method for determination of photo-induced electron and hole transport in electro-optic crystals," Sol. Stat. Commun. **27**, 1351 (1978).

[49] A. M. Glass, D. von der Linde, and T. J. Negran, "High-voltage bulk photovoltaic effect and the photorefractive process in $LiNbO_3$," Appl. Phys. Lett. **25**, 233 (1974).

[50] R. Herrmann and U. Preppernau, *Elektronen im Kristall* (Springer-Verlag Wien New York, 1979).

[51] K. Buse and K. H. Ringhofer, "Pyroelectric drive for light-induced charge transport in the photorefractive process," Appl. Phys. A **57**, 161 (1993).

[52] K. Brands, M. Falk, D. Haertle, T. Woike, and K. Buse, "Impedance spectroscopy of iron-doped lithium niobate crystals," Appl. Phys. B **91**, 279 (2008).

[53] L. Arizmendi, P. D. Townsend, M. Carrascosa, J. Baquedano, and J. M. Cabrera, "Photorefractive fixing and related thermal effects in $LiNbO_3$," J. Phys. Condens. Matt. **3**, 5399 (1991).

[54] N. V. Kukhtarev, "Kinetics of hologram recording and erasure in electrooptic crystals," Sov. Tech. Phys. Lett. **2**, 438 (1976).

[55] N. V. Kukhtarev, V. B. Markov, S. G. Odoulov, M. S. Soskin, and V. L. Vinetskii, "Holographic storage in electrooptic crystals," Ferroelectrics **22**, 949 (1979).

[56] M. Kösters, B. Sturman, D. Haertle, and K. Buse, "Kinetics of photorefractive recording for circular light beams," Opt. Lett. **34**, 1036 (2009).

[57] P. Günther and J.-P. Huignard, *Topics in Applied Physics: Photorefractive Materials and Their Applications I / II* (Springer Verlag Berlin Heidelberg, 1988).

[58] M. Jazbinšek and M. Zgonik, "Material tensor parameters of $LiNbO_3$ relevant for electro- and elasto-optics," Appl. Phys. B **74**, 407 (2002).

[59] F. Jermann and J. Otten, "Light-induced charge transport in $LiNbO_3$:Fe at high light intensities," J. Opt. Soc. Am. B **10**, 2085 (1993).

[60] G. De la Paliza, O. Caballero, A. García-Cabañes, M. Carrascosa, and J. M. Cabrera, "Superlinear photovoltaic currents in proton-exchanged $LiNbO_3$ waveguides," Appl. Phys. B **76**, 555 (2003).

[61] J. Carnicero, O. Caballero, M. Carrascosa, and J. M. Cabrera, "Superlinear photovoltaic currents in $LiNbO_3$: analyses under the two-center model," Appl. Phys. B **79**, 351 (2004).

[62] M. Kösters, C. Becher, D. Haertle, B. Sturman, and K. Buse, "Charge transport properties of undoped congruent lithium niobate crystals," Appl. Phys. B **97**, 811 (2009).

[63] O. Althoff and E. Krätzig, "Strong light-induced refractive index changes in $LiNbO_3$," SPIE Nonlin. Opt. Mater. III **12**, 1273 (1990).

[64] O. Althoff, A. Erdmann, L. Wiskott, and P. Hertel, "The photorefractive effect in $LiNbO_3$ at high light intensity," Phys. Stat. Sol. a **128**, K41 (1991).

[65] J. J. Liu, P. P. Banerjee, and Q. W. Song, "Role of diffusive, photovoltaic, and thermal effects in beam fanning in $LiNbO_3$," J. Opt. Soc. Am. B **11**, 1688 (1994).

[66] R. Magnusso and T. K. Gaylord, "Laser scattering induced holograms in lithium-niobate," Appl. Opt. **13**, 1545 (1974).

[67] Y. Furukawa, K. Kitamura, A. Alexandrovski, R. K. Route, M. M. Fejer, and G. Foulon, "Green-induced infrared absorption in MgO doped $LiNbO_3$," Appl. Phys. Lett. **78**, 1970 (2001).

[68] F. Jermann, M. Simon, and E. Krätzig, "Photorefractive properties of congruent and stoichiometric lithium niobate at high light intensities," J. Opt. Soc. Am. B **12**, 2066 (1995).

[69] M. Carrascosa, J. Villarroel, J. Carnicero, A. García-Cabañes, and J. M. Cabrera, "Understanding light intensity thresholds for catastrophic optical damage in $LiNbO_3$," Opt. Express **16**, 115 (2008).

[70] M. Falk, *Thermo-electric oxidization of iron in lithium niobate crystals*, Ph.D. thesis, University of Bonn (2008).

[71] T. Volk, N. Rubinina, and M. Wöhlecke, "Optical-damage-resistant impurities in lithium niobate," J. Opt. Soc. Am. B **11**, 1681 (1994).

[72] M. C. Wengler, U. Heinemeyer, E. Soergel, and K. Buse, "Ultraviolet light-assisted domain inversion in magnesium-doped lithium niobate crystals," J. Appl. Phys. **98**, 064 104 (2005).

[73] M. Falk, T. Woike, and K. Buse, "Charge compensation mechanism for thermo-electric oxidization of lithium niobate crystals," J. Appl. Phys. **102**, 063 529 (2007).

[74] W. Jösch, R. Munser, W. Ruppel, and P. Würfel, "Photovoltaic effect and the charge transport in $LiNbO_3$," Ferroelectrics **21**, 623 (1978).

[75] K. Buse, S. Breer, K. Peithmann, S. Kapphan, M. Gao, and E. Krätzig, "Origin of thermal fixing in photorefractive lithium niobate crystals," Phys. Rev. B **56**, 1225 (1997).

[76] J. M. Cabrera, J. Olivares, M. Carrascosa, J. Rams, R. Müller, and E. Diegues, "Hydrogen in lithium niobate," Adv. Phys. **45**, 349 (1996).

[77] S. Klauer, M. Wöhlecke, and S. Kapphan, "Influence of H-D isotopic substitution on the protonic conductivity of $LiNbO_3$," Phys. Rev. B **45**, 2786 (1992).

[78] K. Peithmann, A. Wiebrock, and K. Buse, "Photorefractive properties of highly doped lithium niobate crystals in the visible and near-infrared," Appl. Phys. B **68**, 777 (1999).

[79] B. I. Sturman, M. Carrascosa, F. Agulló-López, and J. Limeres, "Theory of high-temperature photorefractive phenomena in $LiNbO_3$ crystals and applications to experiment," Phys. Rev. B **57**, 12 792 (1998).

[80] A. Yariv and P. Yeh, *Optical Waves in Crystals* (Wiley Interscience, 2003).

[81] S. Kapphan and A. Breitkopf, "PE-layers and proton diffusion profiles in $LiNbO_3$ investigated with Fourier-IR and second harmonic generation," Phys. Stat. Sol. a **133**, 159 (1992).

[82] B. Sturman, M. Carrascosa, and F. Agulló-López, "Light-induced charge transport in $LiNbO_3$ crystals," Phys. Rev. B **78**, 245 114 (2008).

[83] Y. Furukawa, K. Kitamura, S. Takekawa, A. Miyamoto, M. Terao, and N. Suda, "Photorefraction in $LiNbO_3$ as a function of [Li]/[Nb] and MgO concentrations," Appl. Phys. Lett. **77**, 2494 (2000).

[84] G. D. Miller, R. G. Batchko, W. M. Tulloch, D. R. Weise, M. M. Fejer, and R. L. Byer, "42%-efficient single-pass cw second-harmonic generation in periodically poled lithium niobate," Opt. Lett. **22**, 1834 (1997).

Acknowledgements

My sincere gratitude goes to Prof. Dr. Karsten Buse for his deep trust in me throughout my academic carrier and for his great support during my studies abroad at the California Institute of Technology, during my diploma thesis, and, finally, during my PhD thesis. He provided an excellent working environment and was always open for discussions.

I thank Prof. Dr. Karl Maier for his kind readiness to take over the primary review of my thesis. Thanks also to PD Dr. Bernard Metsch and Prof. Dr. Werner Mader for the secondary reviews.

Special thanks go to Prof. Dr. Boris Sturman – his great analytical skills and his profound knowledge strongly influenced this thesis – and to PD Dr. Theo Woike, Dr. Daniel Haertle, and Dr. Konrad Peithmann, who supported me with fruitful discussions and inspiring ideas.

I am much obliged to Patrick Werheit and Carsten Becher, who carried out their diploma thesis on the "optical cleaning" project, for their excellent contributions.

Thanks also to the entire "Hertz" team: Dr. Akos Hoffmann helped with technical, especially electronic, challenges. Ms. Raja Bernard took care of all administrative issues. All former and current members of the "Hertz" group, especially of the "Eckbüro", created an enjoyable working atmosphere and were always up for interesting discussions about and beyond physics. I will surely miss this pleasant and inspiring ambience.

Furthermore, I thank the workshops for fabricating custom-designed parts of the experimental setups. In particular, I appreciate the work of Jürgen Vorzepf and Ulrich Böhning for grinding and polishing the crystals, which have been used to conduct the experiments.

Special thanks go to my girlfriend Cornelia Monzel, who enriched the last year of my PhD studies simply with her presence.

Last but not least, I am deeply grateful to my brother Markus and to my parents, Brigitte and Norbert Kösters, for their incredible support not only with respect to my studies, but throughout all aspects of my life.

List of publications

- B. Sturman, M. Kösters, D. Haertle, C. Becher, and K. Buse, "Optical cleaning owing to the bulk photovoltaic effect," Phys. Rev. B **80**, 245319 (2009).
- M. Kösters, C. Becher, D. Haertle, B. Sturman, and K. Buse, "Charge transport properties of undoped congruent lithium niobate crystals," Appl. Phys. B **97**, 811 (2009).
- M. Kösters, B. Sturman, P. Werheit, D. Haertle, and K. Buse, "Optical cleaning of congruent lithium niobate crystals," Nat. Phot. **3**, 510 (2009).
- M. Kösters, B. Sturman, D. Haertle, and K. Buse, "Kinetics of photorefractive recording for circular light beams," Opt. Lett. **34**, 1036 (2009).
- L. Jentjens, H. Hattermann, K. Peithmann, M. Haaks, K. Maier, and M. Kösters, "Domain reversal properties and refractive index changes of magnesium doped lithium niobate upon ion exposure," J. Appl. Phys. **103**, 034104 (2008).
- O. Caballero-Calero, M. Kösters, T. Woike, K. Buse, A. García-Cabañes, and M. Carrascosa, "Electric field periodical poling of lithium niobate crystals after soft-proton-exchanged waveguide fabrication," Appl. Phys. B **88**, 75 (2007).
- U. Hartwig, M. Kösters, T. Woike, and K. Buse, "High-temperature-recorded index gratings in periodically-poled lithium niobate," Opt. Lett. **31**, 3267 (2006).
- M. Kösters, U. Hartwig, T. Woike, K. Buse, and B. Sturman, "Quantitative characterization of periodically poled lithium niobate by electrically induced Bragg diffraction," Appl. Phys. Lett. **88**, 182910 (2006).
- U. Hartwig, M. Kösters, T. Woike, K. Buse, S. Shumelyuk, and S. Odoulov, "Frequency mixing of photorefractive and ferroelectric gratings in lithium niobate crystals," Opt. Lett. **31**, 583 (2006).
- M. Kösters, H. T. Hsieh, D. Psaltis, and K. Buse, "Holography in commercially available photo-etchable glasses," Appl. Opt. **44**, 3399 (2005).